Segment-scale variations in the crustal structure of 150–300 kyr old fast spreading oceanic crust (East Pacific Rise, 8°15′N–10°5′N) from wide-angle seismic refraction profiles

J. Pablo Canales,[1,*] Robert S. Detrick,[1] Douglas R. Toomey[2] and William S. D. Wilcock[3]

[1]*Department of Geology and Geophysics, Woods Hole Oceanographic Institution,* 360 *Woods Hole Rd, Woods Hole,* MA 02543, *USA.*
E-mail: jpcanales@whoi.edu
[2]*Department of Geological Sciences, University of Oregon, Eugene,* OR 97403, *USA*
[3]*School of Oceanography, University of Washington, Seattle,* WA 98195, *USA*

Accepted 2002 October 3. Received 2002 October 1; in original form 2001 October 1

SUMMARY

We have simultaneously inverted seismic refraction and wide-angle Moho reflection traveltimes for the 2-D crustal thickness and velocity structure of 150–300 kyr old crust along the East Pacific Rise (EPR) between the Siqueiros and Clipperton fracture zones (FZs). Our results show a strong correlation between ridge segmentation and upper- and mid-crustal seismic velocities, with higher velocities near segment centres and lower velocities near segment ends. Low crustal velocities at the Clipperton and Siqueiros FZs are interpreted as fracturing resulting from brittle deformation of the crust in the transform domain. A relict overlap basin left on the Pacific Plate by the 9°03′N overlapping spreading centre (OSC) as it propagated southward is associated with a large ($\sim$1 km s^{-1}), negative upper- and mid-crustal velocity anomaly. This anomaly is consistent with the presence of an unusually thick extrusive section within the basin and with tectonic alteration, fracturing and shearing arising from rotation of the basin as it was formed. The discordant zone left by this OSC on the Cocos Plate is characterized by moderately low crustal velocities, probably because of crustal fracturing as the OSC propagated into older crust. Higher crustal velocities near segment centres may reflect a higher ratio of dikes to extrusives in the upper crust, and lower-intensity tectonic alteration of the crust, than near segment ends.

The mean crustal thickness along the EPR between the Siqueiros and Clipperton FZs is 6.7–6.8 km. The thickest crust is found beneath the Lamont seamounts ($\sim$9 km), and in a southward-pointing, V-shaped band located just north of the off-axis trace of the 9°03′N OSC (7.3–7.8 km). The thinnest crust ($<$6 km) is found proximal to the Clipperton and Siqueiros FZs. The crust associated with the off-axis trace of the 9°03′N OSC is not anomalously thin, suggesting that magma supply beneath the OSC is similar to that of the northern and southern segments. We see a similar pattern of crustal thickness variation to that determined using multichannel reflection data, including a gradual thickening of the crust from north to south along the northern ridge segment, and the location of the thickest crust just north of the 9°03′N OSC. However, the magnitude of the along-axis crustal thickness variation we observe along the northern ridge segment between 9°50′N and 9°15′N ($\sim$1.3–1.8 km, excluding the Lamont seamounts) is significantly less than the 2.3 km of variation previously reported, weakening the case for the existence of a low-density mantle diapir at 9°50′N inferred from gravity data. The band of thick crust located just north of the off-axis trace of the 9°03′N OSC suggests a close genetic link between this feature and the OSC. Thus we attribute the pattern of crustal thickness variations along the northern segment to the kinematics of the southward-propagating 9°03′N OSC over the past 0.5 Myr, and not to along-axis melt migration away from a mantle diapir as previously proposed.

Key words: crustal structure, East Pacific Rise, mid-ocean ridge, oceanic crust, overlapping spreading centres, seismic tomography.

*Corresponding author.

1 INTRODUCTION

The thickness of oceanic crust formed at oceanic spreading centres reflects the amount of melt extracted from the upwelling mantle, accumulated during the time that a crustal column is exposed to the melt supply system (e.g. Forsyth 1992). Seismic measurements suggest that crustal thickness variability is spreading-rate dependent with crust formed at slow spreading rates (<30 mm yr^{-1} full rate), displaying much greater variability in thickness than crust formed at fast spreading rates (>50 mm yr^{-1} full rate) (e.g. White *et al.* 1992). At slow spreading ridges, such as the Mid-Atlantic Ridge (MAR), the full range of crustal thickness variation predicted by the large, along-axis variation in mantle Bouguer gravity anomaly (MBA) (e.g. Lin *et al.* 1990; Detrick *et al.* 1995) is observed within a single tectonically defined ridge segment (e.g. Tolstoy *et al.* 1993; Canales *et al.* 2000; Hooft *et al.* 2000). In contrast, the MBA along fast spreading ridges, such as the East Pacific Rise (EPR), have relatively small amplitudes (e.g. Madsen *et al.* 1990), suggesting little along-axis crustal thickness variation. Although no comprehensive seismic refraction studies of segment-scale crustal thickness variation have been carried out at fast spreading ridges, the available data (e.g. Canales *et al.* 1998) are consistent with the view that crust formed at fast spreading ridges is more uniform in thickness than crust formed along slow spreading ridges.

This spreading-rate dependence of crustal thickness and MBA variations has been explained by two fundamentally different modes of mantle upwelling beneath mid-ocean ridges (Lin & Phipps Morgan 1992). In one model there is a strong spreading-rate dependence to the pattern of mantle upwelling with focused, buoyantly driven, diapiric flow beneath slow spreading ridges but more sheet-like, 2-D, plate-driven flow beneath fast spreading ridges (Parmentier & Phipps Morgan 1990; Lin & Phipps Morgan 1992). An important implication of this model is that crustal magma chambers at fast spreading ridges can be supplied from below at closely spaced intervals along the entire length of a ridge segment without significant along-axis redistribution of magma. An alternative hypothesis is that mantle upwelling is highly focused and diapiric at all spreading rates, but there is a more efficient along-axis distribution of melt at crustal and sub-Moho levels at fast spreading ridges, or ductile deformation of the hot, lower crust, which smooths out any initial differences in crustal thickness (Bell & Buck 1992; Wang & Cochran 1993). This hypothesis is more consistent with localized, widely spaced centres of magma injection into the crust as proposed for the EPR by Macdonald *et al.* (1991) and Batiza & Niu (1992) based on morphologic and petrologic data.

Studies along the EPR between the Clipperton and Siqueiros fracture zones that directly imaged the axial structure have shown that the axial magma plumbing system is segmented at a scale of 10–20 km at both crustal and shallow mantle levels, providing strong evidence for a 2-D pattern of mantle flow (Toomey *et al.* 1990; Harding *et al.* 1993; Kent *et al.*1993a,b, 2000; Dunn *et al.* 2000, 2001). However, crustal thickness variations in this area are larger than that predicted by a simple 2-D model of mantle flow. Barth & Mutter (1996) report crustal thickness variations of 2.6 km between 9°50′N and 8°50′N based on their interpretation of Moho reflection times observed in multichannel seismic reflection (MCS) data, although along-axis MBA gradients between the Clipperton and Siqueiros fracture zones are very small (Madsen *et al.* 1990; Wang *et al.* 1996). Even more surprisingly, they found thin crust (5.0 km) associated with the shallowest, broadest section of the ridge near 9°50′N and the thickest crust (>7 km) located just north of the overlapping spreading centre (OSC) at 9°03′N near the southern end of this segment. In order to reconcile these crustal thickness variations with the small along-axis MBA gradients observed along the ridge, Wang *et al.* (1996) proposed the presence of a low-density, melt-rich, mantle diapir beneath the EPR at ∼9°50′N. A similar pattern of thin crust overlying a mantle diapir with crustal thickening away from the upwelling centre has been reported from the Oman ophiolite (Nicolas *et al.* 1996), which is also inferred to have formed at a fast spreading ridge (e.g. MacLeod & Rothery 1992).

The discrepancy between inferences from studies of the axial magmatic system and broader-scale studies of gravity and near-axis crustal thickness raises questions concerning the extent to which crustal thickness measurements along fast spreading ridges are valid indicators of magmatic segmentation, and points to a more complex linkage between the pattern of mantle flow, tectonic segmentation, the axial magma plumbing system and the resulting ocean crustal thickness. In this paper we use seismic refraction and wide-angle Moho reflection traveltimes to determine variations in crustal velocity and crustal thickness on 150–300 kyr old crust along the EPR between the Siqueiros and Clipperton fracture zones. We discuss the implications of our results on the relationship between crustal structure and tectonic segmentation, and on models for magma supply and the role of migrating discontinuities in crustal accretion processes at fast spreading ridges.

2 GEOLOGICAL SETTING

The EPR between the Clipperton and Siqueiros transforms (Fig. 1) is the most extensively studied section of any fast spreading mid-ocean ridge. The full spreading rate increases from 111 mm yr^{-1} at the Clipperton fracture zone (FZ) to 120 mm yr^{-1} at the Siqueiros FZ (Klitgord & Mammerickx 1982). These two fracture zones bound a mid-ocean ridge segment that is further divided into two segments (hereinafter referred to as the northern and southern segments) by the 9°03′N OSC (Macdonald *et al.* 1992). Both segments are believed to be magmatically active, as inferred from morphological observations (Macdonald & Fox 1988; Scheirer & Macdonald 1993), the along-axis continuity and brightness of a crustal reflector interpreted as the top of an axial magma chamber (Herron *et al.* 1980; Detrick *et al.* 1987; Kent *et al.* 1993a), the presence of crustal and upper-mantle low-seismic-velocity and high-attenuation zones (Toomey *et al.* 1990, 1994; Wilcock *et al.* 1992, 1995; Dunn & Toomey 1997; Dunn *et al.* 2000), and the abundance of hydrothermal vents (Haymon *et al.* 1991).

The segment discontinuity at 9°03′N (Fig. 1) is formed by an 8 km wide, 27 km long OSC encompassing a 500 m deep overlap basin (Macdonald & Fox 1983; Sempéré & Macdonald 1986; Sempéré *et al.* 1984). The offset has widened during the last 1 Myr from 2 to 8 km, and the OSC has migrated southward since 1.8 Ma (Carbotte & Macdonald 1992), leaving an off-axis, V-shaped discordant zone (Fig. 1) similar to those observed in other areas of the EPR (e.g. Lonsdale 1989). The western flank of the V-shaped trace (Pacific Plate) consists of rotated (>25°), discrete relict overlap basins, while the eastern flank (Cocos Plate) is a broad, deeper discordant zone formed by anomalous lineations (Carbotte & Macdonald 1992). A 3-D MCS reflection study of the 9°03′N OSC (Kent *et al.* 2000) imaged crustal magma bodies beneath both limbs of the OSC and ponding of melt at crustal depths beneath large areas of the overlap basin. A 3-D mantle refraction study of the OSC (Dunn *et al.* 2001) reveals a continuous ∼20 km wide region of high

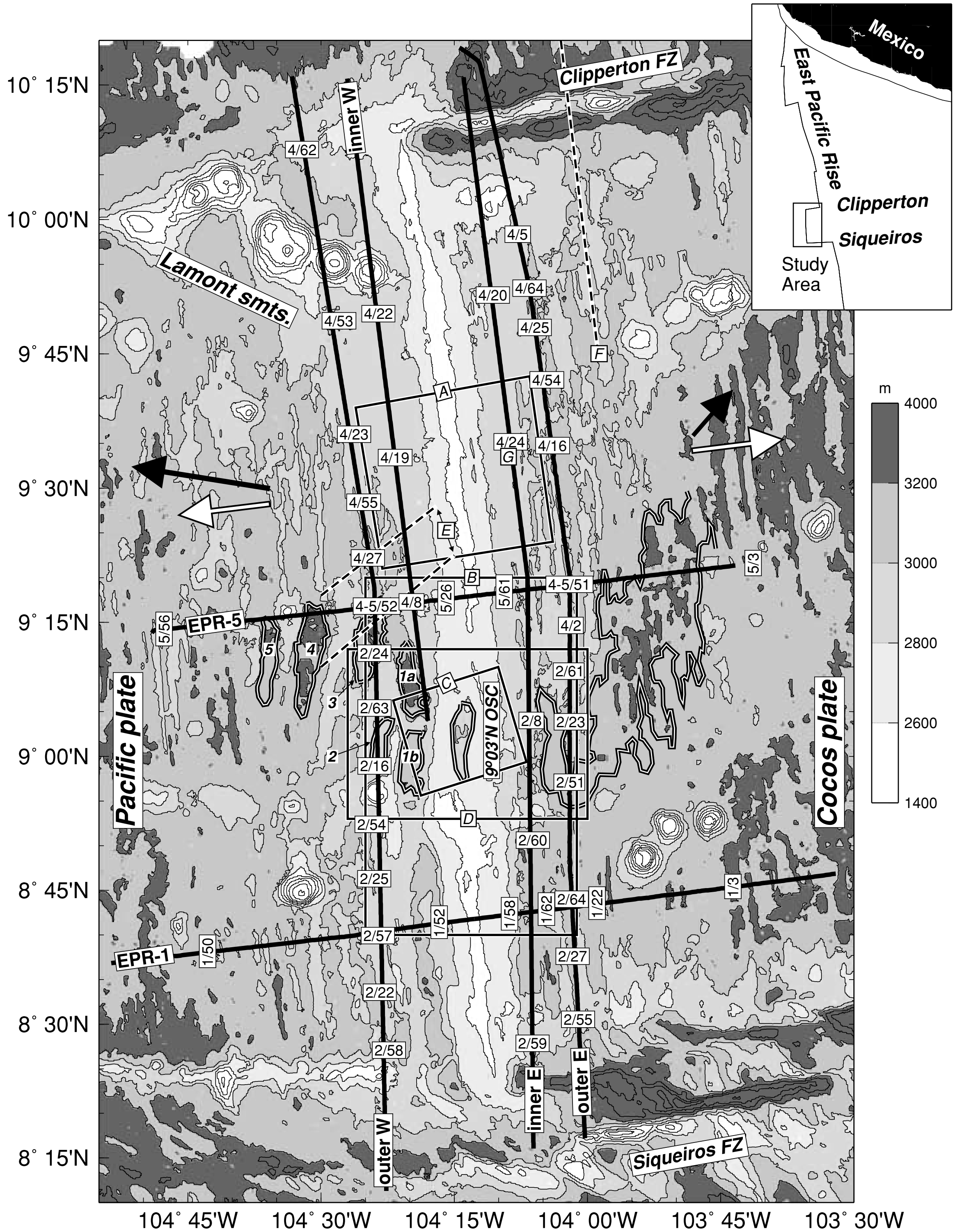

Figure 1. Bathymetry map of the EPR between the Clipperton and Siqueiros fracture zones, contoured every 200 m. Labelled thick solid lines are shooting lines from the Undershoot Seismic Experiment (Toomey *et al.* 1998) for the wide-angle seismic profiles presented in this study. Numbered white boxes show the location of the ocean-bottom seismic instruments. The location of some relevant seismic experiments conducted in the area are shown: 3-D wide-angle seismic refraction (boxes *A* (Toomey *et al.* 1990; 1994; Wilcock *et al.* 1992, 1995; Dunn & Toomey 1997; Dunn *et al.* 2000), *B* (Dunn *et al.* 2001) and *D* (Bazin *et al.* 2001)), 3-D multichannel seismic reflection (box *C* (Kent *et al.* 2000)); 2-D seismic profiles (dashed lines *E* (Christeson *et al.* 1997) and *F* (Begnaud *et al.* 1997; van Avendok *et al.* 1998)); and *G* is the mid-point of ESP-1 (Vera *et al.* 1990). The solid black–white lines show the relict overlap basins (western flank, numbered following the nomenclature of Carbotte & Macdonald (1992)) and the broad discordant zone (eastern flank) left by the southern migration of the 9°03′N OSC (Carbotte & Macdonald 1992). Other geological features such as the Clipperton and Siqueiros FZ and the Lamont Seamounts (Fornari *et al.* 1984) are labelled. Absolute (HS2-NUVEL1 model (Gripp & Gordon 1990)) and relative (NUVEL-1 global plate model (DeMets *et al.* 1990)) plate motion vectors are shown in thick black and white arrows, respectively. The top right-hand inset shows the location of the study area in a broader context.

temperatures and a few per cent melt in the uppermost mantle. Both studies concluded that the opposing limbs of the OSC share a common magma supply at mantle depths and that tectonic segmentation of the rise by the OSC is not a result of magmatic segmentation in the mantle.

The seismic structure of off-axis, young crust in the study area has been studied with a variety of seismic methods. Vera *et al.* (1990) reported the crustal structure of 180 kyr old Cocos crust at 9°35′N from an expanding spread profile (ESP) (Fig. 1). Their 1-D structure consists of a 0.6 km thick upper crust of high-velocity gradients (2.05–5.6 km s^{-1}), a 2.4 km thick mid-crust with more moderate velocity gradients (5.6–7.25 km s^{-1}) and a low-velocity zone, and a constant-velocity (7.25 km s^{-1}) 3.8 km thick lower crust. This 6.8 km thick crust is underlain by a 1.4 km thick Moho transition zone. The detailed structure of the uppermost 0–120 kyr old crust has been studied from MCS (Harding *et al.* 1993; Vera & Diebold 1994) and on-bottom refraction data (Christeson *et al.* 1994), indicating a layer 2A thickness of 200–500 m. Seismic measurements across the Clipperton FZ indicate the presence of a 5.7 km thick crust with anomalously low crustal seismic velocities (1 km s^{-1} lower than the average in the area) attributed to brittle deformation and fracturing of the crust (Begnaud *et al.* 1997; van Avendok *et al.* 1998, 2001).

Barth & Mutter (1996) published an extensive study of crustal thickness variation in this area, estimated from two-way traveltimes (TWTT) of Moho reflections interpreted on MCS profiles (Fig. 2). They report a total range of crustal traveltimes between ∼9°50′N and 8°50′N of 1.55–2.45 s. Although Moho TWTT may reflect changes in either crustal velocity or thickness (or both), these authors interpreted their results in terms of crustal thickness variations accommodated within seismic layer 3. Their results suggest that crustal thickness in the area may vary by ∼2.6 km. The thickest crust (7.3 km) was found between 9°10′N and 9°20′N, immediately to the north of the 9°03′N OSC (Fig. 2). The thinnest crust was found near 9°50′N (5.0 km), and also locally beneath the OSC discordant zone (4.7 km).

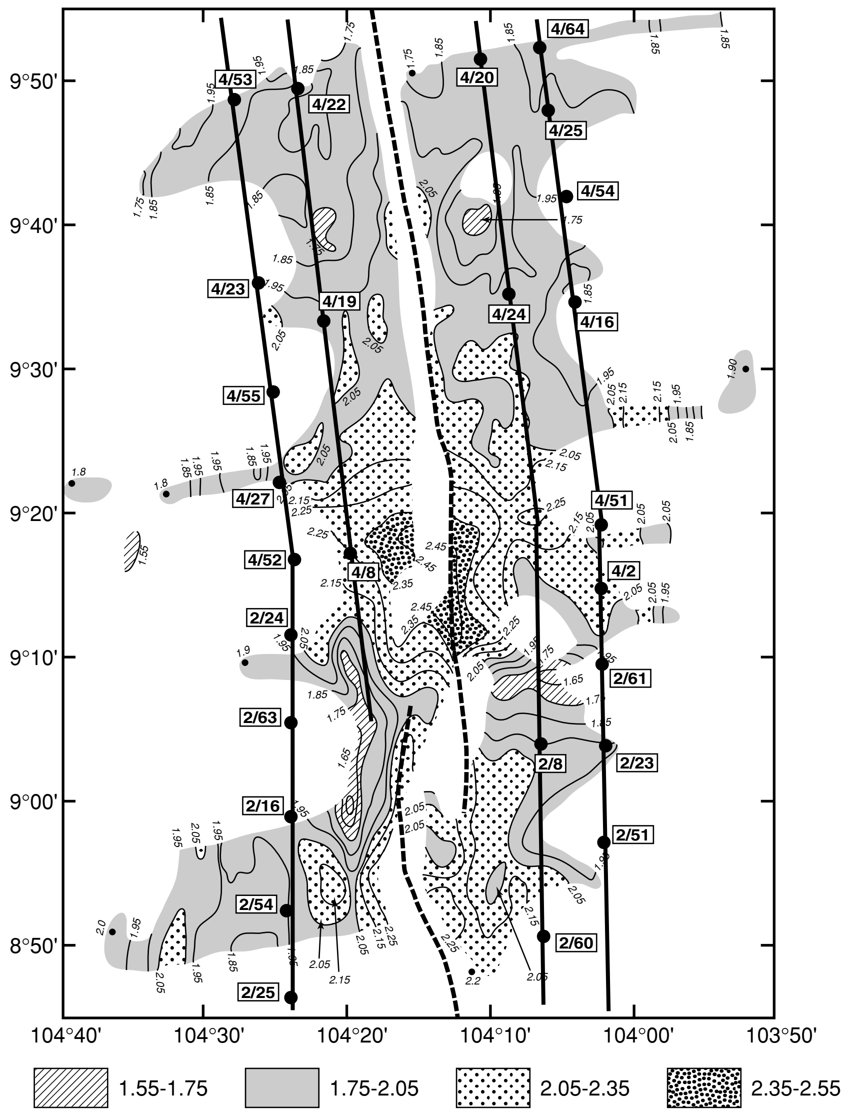

Figure 2. Contour map of the seafloor-to-Moho reflection TWTT along the EPR between 8°50′N and 9°50′N (modified from Barth & Mutter 1996). Shading and contours annotated in seconds. Solid lines and labelled solid circles are the seismic profiles and some of the instruments used in this study (see Fig. 1). The dashed line corresponds to the rise axis. Note the increase in TWTT between ∼9°05′N and ∼9°25′N, which suggests thicker crust immediately to the north of the 9°03′N OSC.

Table 1. Number of instruments, shots and traveltime picks for each profile.

Line	Number of instruments[a] OBH/ORB	OBS	Number of air gun shots		Number of traveltime picks *Pg*	*PmP*
			Deployment 2	Deployment 4		
Outer western	6 (7)	8 (9)	389	321	2524	785
Inner western	3	0	–	302	368	119
Inner eastern	3 (4)	2	290	331	806	346
Outer eastern	6 (8)	7 (9)	289	328	1991	480
			Deployment 1	Deployment 5		
West EPR-5[b]	1 (2)	2	–	152	242	161
East EPR-5[b]	0 (1)	3	–	122	261	124
West EPR-1[b]	0 (1)	2 (3)	193	–	209	137
East EPR-1[b]	2	2	188	–	447	288

[a]Numbers of instruments used in this study (the total number of instruments deployed is indicated in parentheses, when they differ). OBH: ocean-bottom hydrophone; ORB: ocean reftek in a ball (hydrophone); OBS: ocean-bottom seismometer (three-component seismometer plus hydrophone).
[b]Although the instruments along EPR-5 and EPR-1 recorded data from shots at both sides of the ridge axis, only shot–receivers pairs located in the same tectonic plate were used in this study (hence the distinction between east and west).

3 SEISMIC EXPERIMENT

As part of the Undershoot Seismic Experiment (1997 November–December) (Toomey *et al.* 1997), six wide-angle, ocean-bottom seismic refraction experiments were carried out on the flanks of the EPR between the Siqueiros and Clipperton transforms (Fig. 1). The two primary axis-parallel profiles (hereinafter referred to as the outer lines) were ∼230 km long located on ∼300 kyr old crust. Two secondary axis-parallel profiles (hereinafter referred to as the inner lines) were located between the rise axis and the outer lines, on ∼150 kyr old crust. The western and eastern inner lines were ∼135 and ∼225 km long, respectively. Two additional profiles across the rise axis were located along ∼300–800 kyr old crust at latitudes of ∼9°15′N (∼130 km long, referred to as EPR-5) and ∼8°40′N (∼150 km long, referred to as EPR-1) (Fig. 1). The number and type of instruments used in each profile are listed in Table 1. The instruments denoted by '2/' (Fig. 1) recorded data from air gun shots fired between ∼8°10′N and ∼9°35′N along the axis-parallel lines (deployment 2, Table 1). The instruments denoted by '4/' (Fig. 1) recorded data from air gun shots fired between ∼8°55′N and ∼10°15′N along the axis-parallel lines (deployment 4, Table 1). The instruments denoted by '1/' and '5/' (Fig. 1) recorded data from air gun shots fired along the cross-axis lines EPR-1 and EPR-5, respectively (deployments 1 and 5, Table 1). Two of the instruments recorded data from both deployments, 4 and 5 (denoted by '4–5/,' Fig. 1).

The seismic source was the R/V *Maurice Ewing*'s 8503 in^3 (139 l) air gun array (firing pressure of ∼14 MPa) towed at a depth of ∼10 m. Shots were fired at an interval of 210 s (except along the outer western line south of ∼9°35′N and along EPR-1, where the shot interval was 180 s), providing a seismic trace spacing of ∼485 m at a nominal speed of 4.5 knots. Shot positions were obtained from the shipboard Global Positioning System (GPS) position, corrected for the distance between the GPS antenna and the air gun array (87 m). Accurate locations of the instruments on the seafloor (Toomey *et al.* 1997) were determined by inverting the direct water wave traveltimes (for ranges ≤12 km) using the method of Creager & Dorman (1982). The velocity–depth function of the water column was obtained from temperature measurements with expendable bathythermograph probes. The water depths at the relocated positions were obtained from the Hydrosweep multibeam bathymetry.

4 DATA AND SEISMIC MODELLING

The seismic data were recorded by the OBSs and OBH/ORBs (Table 1) at 128 and 200 samples s^{-1}, respectively, and reduced to the standard format of the Society of Exploration Geophysicists (SEG-Y) after correcting for the time drift of the internal clock of the instruments. For plotting and interpretation purposes we applied a bandpass filter of 5–20 Hz to the record sections. In Fig. 3 we show four illustrative record sections. Seismic arrivals in data with high signal-to-noise ratio can be identified at shot–receiver ranges of up to 100 km. At offsets ≤50 km, we have identified first arrivals attributed to *P*-wave refractions within the crust (*Pg*) and high-amplitude, secondary arrivals attributed to *P*-wave reflections from the Moho (*PmP*). Refractions in the uppermost mantle (*Pn*) were most clearly observed in the across-axis profiles (Fig. 3d). *Pn* arrivals on the axis-parallel profiles are difficult to observe owing to the presence of 5–7 per cent azimuthal mantle anisotropy (Dunn *et al.* 2001), which results in *Pn* energy propagating parallel to the ridge at seismic velocities only slightly faster than lower-crustal velocities. Thus we have not included *Pn* arrivals in our analysis, and we have limited the shot–receiver range to ≤50 km to avoid modelling possible *Pn* refractions as *PmP* reflections.

Our analysis is based on the joint inversion of *Pg* and *PmP* traveltime data for the 2-D *P*-wave crustal velocity model and depth to Moho. We applied the method of Korenaga *et al.* (2000), a joint refraction and reflection traveltime tomography inversion that simultaneously solves for the seismic velocity field and the depth of a reflecting interface. The forward problem is solved by a hybrid method based on the shortest path (e.g. Moser 1991) and the ray-bending (e.g. Moser *et al.* 1992) methods, and the inverse problem uses a sparse least-squares method (Paige & Saunders 1982) to solve a regularized linear system. The traveltimes were hand-picked (Table 1), with a mean uncertainty of 25 ms. The model is parametrized as a sheared mesh hanging from the seafloor topography with 0.4 km lateral nodal spacing and variable vertical nodal spacing (0.1 km within the upper 2 km and increasing to 0.5 km at depths >7 km). The Moho is parametrized as a floating reflector with nodes every 2 km with one degree of freedom in the vertical direction. The method of Korenaga *et al.* (2000) uses weighted correlation lengths to impose smoothing constraints. For the velocity nodes we used a depth-dependent horizontal correlation length that increases linearly from 3 km at the seafloor to 8 km at the bottom

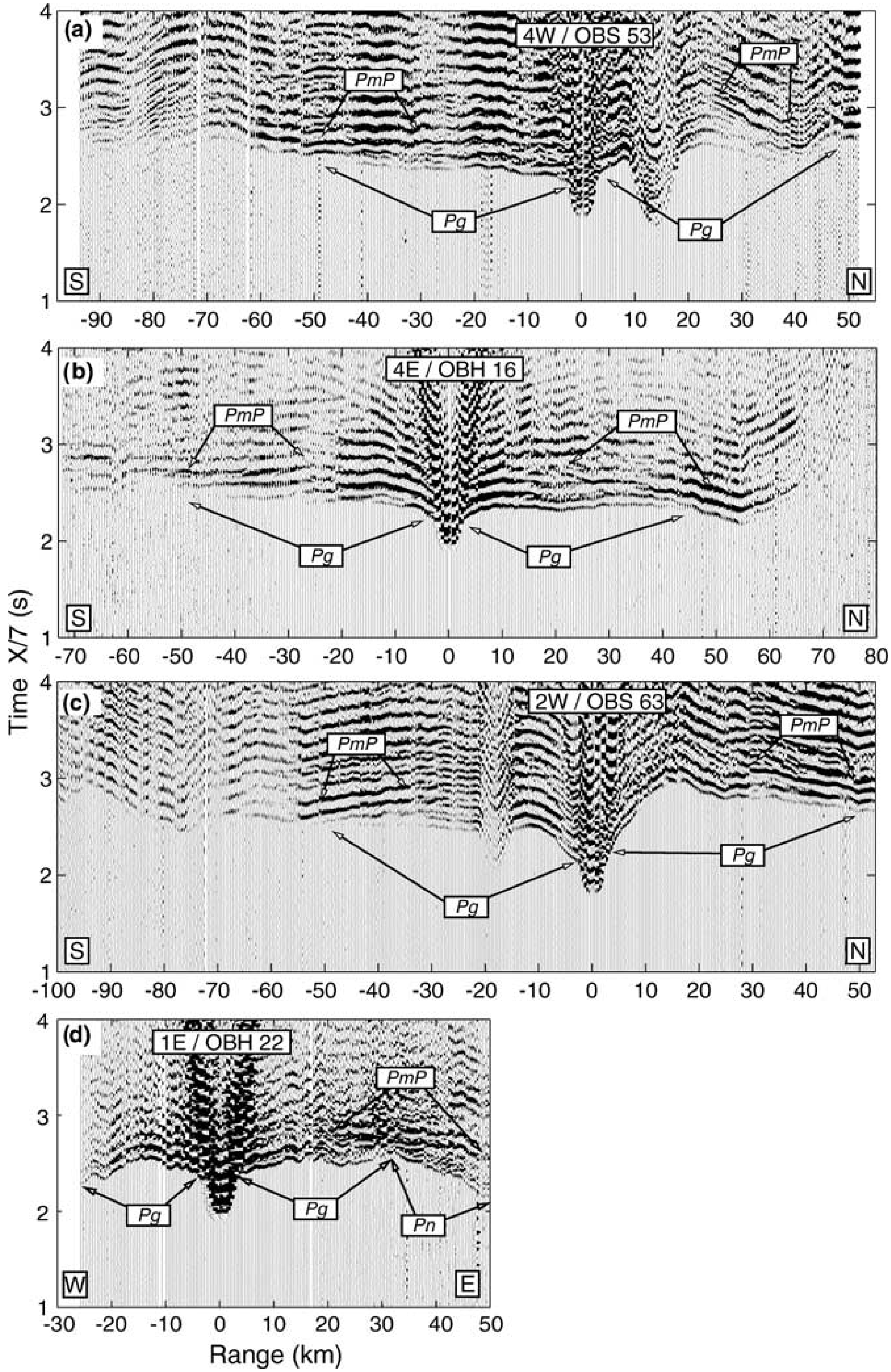

Figure 3. The observed seismic record sections from some selected instruments. Vertical axes are the reduced traveltime in seconds and horizontal axes are shot–receiver offset in kilometres. Data have been reduced to 7 km s^{-1} and bandpass filtered between 5 and 20 Hz. No topographic corrections have been applied. Amplitudes have been scaled with range using a power-law gain. Labels and arrows show the seismic phases (*Pg,* crustal turning rays; *PmP,* Moho reflections; *Pn,* upper-mantle refractions).

of the model (15 km subseafloor depth), and a vertical correlation length that also increases linearly from 0.5 km at the seafloor to 1 km at the bottom, both weighted by a factor of 200. The correlation length for the depth nodes of the reflector is 8 km, weighted by a factor of 15. Also, the depth sensitivity is weighted by a depth kernel weighting parameter (w). The large number of traveltime picks and the close spacing of the instruments along the two primary axis-parallel lines justifies the adoption of an equal weighting of velocity and depth nodes ($w = 1$) (Korenaga *et al.* 2000). For the other profiles where the instruments are more widely and not evenly spaced we adopted a value of $w = 10$.

The starting 1-D velocity model for the axis-parallel profiles is shown in Fig. 4. The layer 2A structure (upper ∼400 m) corresponds to that obtained by Christeson *et al.* (1994) in this same area using on-bottom seismic refraction methods. Below 400 m we chose a seismic structure similar to that obtained by Vera *et al.* (1990), but with less variability within the upper 3 km. For the across-axis profiles we used as initial velocity models the structure obtained along the outer western and eastern lines at the crossing points with EPR-5 and EPR-1. The initial crustal thickness was set to 6 km in all the profiles.

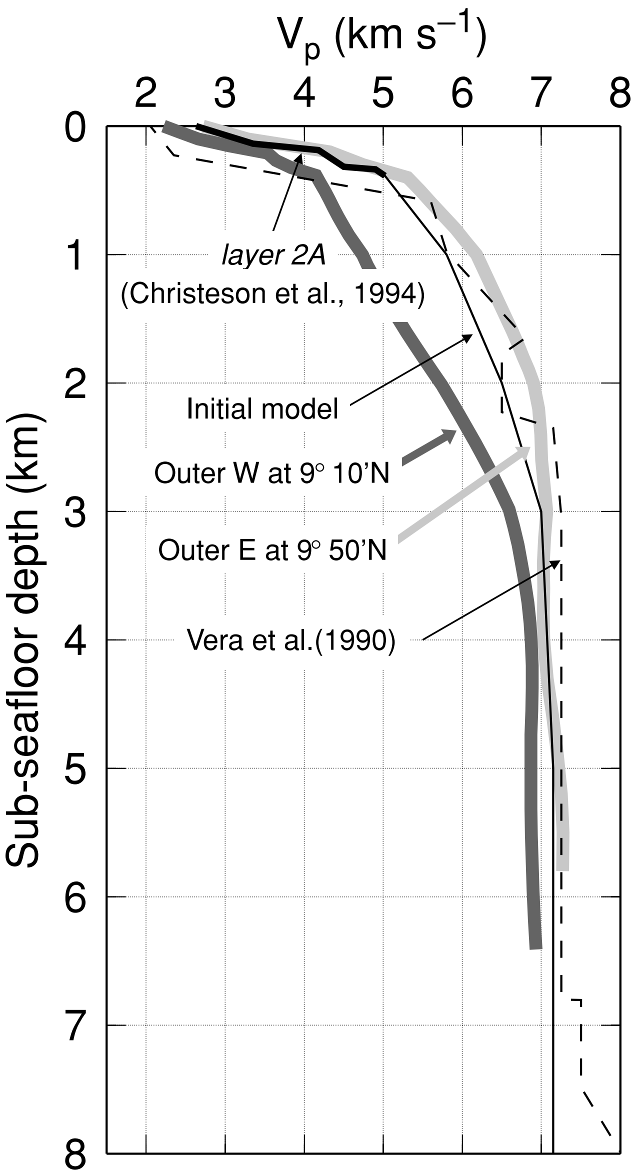

Figure 4. 1-D initial velocity model (solid line). The structure within the upper 400 m (thick solid line) is that obtained from an on-bottom seismic refraction experiment in our study area by Christeson *et al.* (1994). For reference we show the structure obtained by Vera *et al.* (1990) in the area (ESP-1, dashed line). Grey lines show our results obtained along the outer western profile at 9°10′N beneath the relict overlap basin 3 (dark) and along the outer eastern line at 9°50′N (light), averaged over 10 km wide bins.

5 RESULTS

Our preferred 2-D models are presented in this section. The ray sampling and data fitting are discussed in Appendix A, and the resolution of the models is discussed in Appendix B. The inversion method tends to underestimate the amplitude of the velocity anomalies, which should be interpreted as an average imposed by the smoothing constraints.

5.1 Western lines

The 2-D crustal velocity model along the outer western line, and the perturbation with respect to the initial 1-D velocity structure are shown in Figs 5(a) and (e), respectively. Within the uppermost 3 km of the crust, the most prominent feature of the velocity model is the alternating pattern of relatively high velocities within both segments, and lower seismic velocities at the ridge axis discontinuities. The upper crust in the centre of the segments is characterized by positive velocity anomalies of 0.2–0.4 km s^{-1}, while the segment ends bounded by the inactive traces of the Siqueiros and Clipperton FZ have negative upper-crustal velocities anomalies of 0.4–0.6 km s^{-1} (Fig. 5e). A large -1 km s^{-1} velocity anomaly is observed in the upper crust at ∼9°10′N (Fig. 5e), immediately beneath the abandoned overlap basin 3 of Carbotte & Macdonald (1992). Locally, the Lamont seamounts at the northern end of the profile (Fig. 1) are also associated with low upper-crustal velocities.

The depth to Moho along the outer western profile obtained from the inversion shows significant variations at a lateral scale of ∼50 km (Figs 5a and e). The mean crustal thickness along the profile is 6.8 km, with a local maximum of 7.8 km at 9°17′N immediately north of the relict overlap basin. The crust thickens to 9 km beneath the Lamont seamounts.

Although the inner western line samples only the northern part of the study area with just three instruments, the results are consistent with the pattern observed along the outer line (Figs 5b and f). The centre of the northern segment has a 0.2 km s^{-1} positive velocity anomaly within the upper 3 km of the crust, and the crustal thickness is 7.0 km.

5.2 Eastern lines

The preferred 2-D crustal velocity model and the velocity perturbation for the outer eastern line are shown in Figs 5(d) and (h), respectively. The velocity structure on the eastern flank of the EPR shows a similar pattern of relatively high velocities along the middle portions of each segment and lower seismic velocities near the segment discontinuities. Both segments have >0.2 km s^{-1} positive anomalies within the upper 3 km. Both the discordant zone between 9°00′N and 9°10′N, and the Clipperton FZ show a moderate (-0.2 km s^{-1}) negative anomaly, while the Siqueiros FZ has lower seismic velocities (up to -1 km s^{-1} velocity anomaly). The crust along the outer eastern line systematically thickens away from the

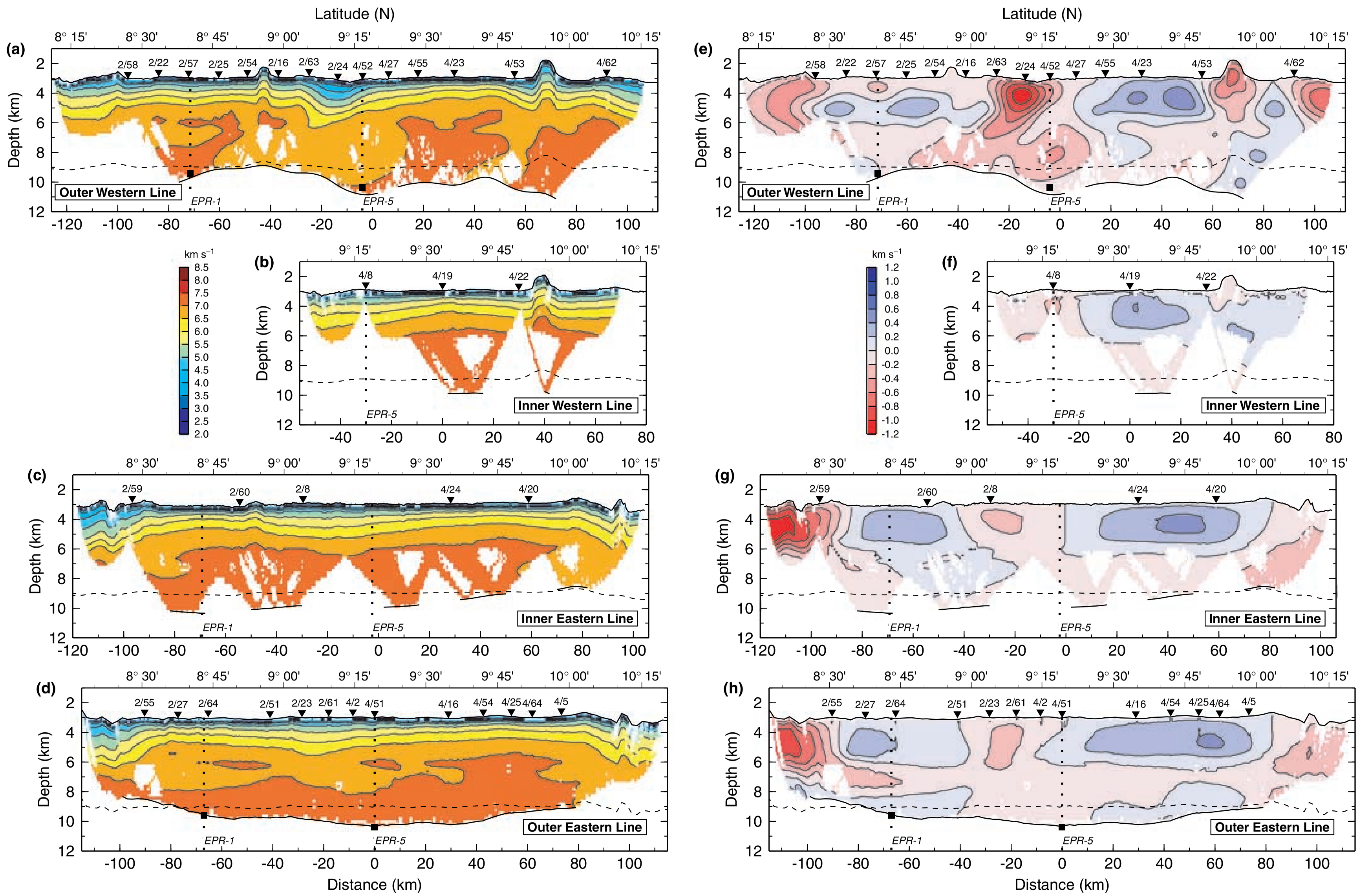

Figure 5. (a)–(d) Final 2-D velocity models. Lower- and upper-horizontal axes represent the distance and the latitude, respectively, along the profile. The profiles are displayed from west to east: (a) outer western line; (b) inner western line; (c) inner eastern line; and (d) outer eastern line. The models have been masked where the ray sampling is non-existent. Velocity contours are every 0.5 km s^{-1}. The colour scale is the same for all the profiles in (a)–(d). The dashed line shows the initial Moho depth (6 km constant crustal thickness), and the solid line is the best-fitting Moho. Only the sections of the modelled Moho where there are *PmP* reflections are shown (see Fig. A1). Numbered triangles are the ocean-bottom instruments. Vertical dotted lines show the crossing points with profiles EPR-1 and EPR-5, and black squares mark the Moho depth determined at these profiles. (e)–(h) Velocity perturbation (final minus initial velocity model) for the same profiles shown in (a)–(d). Contours are every 0.2 km s^{-1}. Scales, labelling and lines are as in (a)–(d). The colour scale is the same for all the profiles in (e)–(h). Note that at upper- and middle-crustal levels, the centre of the segments (from ~8°30′N to 8°55′N and from 9°30′N to 9°50′N) are characterized by relative higher seismic velocities, while segment ends have relative lower seismic velocities. The relict overlap basin at ~9°10′–15′N has very low seismic velocities.

fracture zones (mean crustal thickness of 6.7 km), reaching a maximum thickness of 7.3 km at 9°20′N. The thinnest crust (5.3 km) is found at the Siqueiros FZ.

The crustal velocity structure along the inner eastern line (Figs 5c and g) is similar to that of the outer line. The mean crustal thickness is 6.7 km, as on the outer line. However, the crust along the inner eastern line thickens towards the south, and the thickest crust (7.3 km) is found near the southern end of the segment at 8°40′N.

5.3 Cross-axis lines

The profiles EPR-1 and EPR-5 constrain the crustal structure along flow lines (Fig. 1), and were used to confirm the validity of the along-axis results by comparing the structure at the crossing points. Although the lines were shot across the rise axis with instruments located on both sides of the ridge, we modelled each profile as two separate lines (east and west) including only shot–receivers pairs located on the same side of the ridge. Axial structure determined from rays crossing the ridge axis will be published elsewhere.

Our preferred 2-D crustal velocity model and the velocity perturbation for profile EPR-5 are shown in Figs 6(a) and (b), respectively. There is a pronounced asymmetry in both upper- and lower-crustal velocity structure with respect to the ridge axis, with the Pacific Plate (western ridge flank) displaying lower seismic velocities than the Cocos Plate (eastern ridge flank). The negative upper-crustal velocity anomalies (0.4–0.6 km s^{-1}) on the western flank coincide with the northern limits of the abandoned overlap basins 3, 4 and 5 (see Fig. 1). The crustal velocity asymmetry is consistent with the more pronounced negative velocity anomalies found between 9°00′ and 9°20′N along the outer western line if compared with the outer eastern line (Figs 5e and h).

In contrast, the crustal thickness on the western and eastern ridge flank of EPR-5 is quite symmetric, with mean values of 6.5 and 6.4 km, respectively. There is a pronounced thickening towards the ridge axis, from 5.3 km (west) and 5.9 km (east) at 50 km off-axis to 7.4 km at 20 km off the ridge. The 7.4 km crustal thickness value is comparable to the 7.3 km value found in the outer eastern line near 9°20′N (Fig. 5d), although somewhat lower than the 7.8 km value found in the outer western lines near 9°15′N (Fig. 5a). Fig. 7 shows that the thickest portion of the crust on the Pacific Plate is well sampled in both directions along the outer western and EPR-5 lines, and that the model accurately predicts the observed *PmP* traveltimes.

The structure along EPR-1 (Figs 6c and d) is quite symmetric about the ridge axis. Lower velocities are found near the ridge (0–20 km off-axis) at shallow levels (<2 km below the seafloor), and relatively higher velocities at >20 km off-axis at mid-crustal levels. The mean crustal thickness is 6.3 km, with a slight thickening towards the axis although not as pronounced as in line EPR-5 (6.6 km maximum thickness). The crustal thicknesses at the intersection of EPR-1 and the outer western and eastern lines measured along the three profiles agree well (Figs 5a and d).

6 INTERPRETATION AND DISCUSSION

6.1 *P*-wave crustal velocity structure

The most striking feature of the crustal velocity structure presented in Fig. 5 is the alternating high and low velocities in the upper crust (relative to the starting model, Fig. 4), with higher upper-crustal velocities along the middle of segments and lower crustal velocities at segment ends. First we discuss the implications of this pattern for the structure at segment discontinuities and near segment centres. Then we discuss evidence for seismic crustal anisotropy, and the evolution of the crustal velocity structure inferred from the cross-axis profiles.

6.1.1 Fracture zones and abandoned overlap spreading centres

The eastern lines show that the Siqueiros FZ is characterized by a 1 km s^{-1} negative velocity anomaly, similar to what was reported at the Clipperton FZ by Begnaud *et al.* (1997) and van Avendok *et al.* (2001). As in the latter case, the low seismic velocities found at the Siqueiros FZ are most likely to be caused by extensive fracturing resulting from brittle deformation in the transform domain. In contrast, the eastern lines show a less pronounced velocity anomaly at the Clipperton transform. We attribute this apparent difference in crustal structure between the Clipperton and the Siqueiros FZs to the uneven distribution of instruments, and not necessarily to a significant difference in the actual structure. For example, instruments 2/59 and 2/55 at the southern end of the inner and outer eastern lines, respectively, are located nearer to the Siqueiros transform than instruments 4/20 and 4/5 at the northern end to the Clipperton transform (Fig. 1).

The prominent 1 km s^{-1} negative anomaly found on the outer western line at ∼9°10′N is located beneath the relict overlap basin that bounded both segments ∼300 kyr ago (Carbotte & Macdonald 1992). Low upper-crustal seismic velocities beneath overlap basins have been previously documented in this area (Christeson *et al.* 1997; Bazin *et al.* 2001) and at the southern EPR (Bazin *et al.* 1998). Since both limbs of the 9°03′N OSC are fed by crustal magma chambers (Kent *et al.* 2000), Bazin *et al.* (2001) have proposed that the overlap basin acts as a trap where lavas pond, locally increasing the thickness of layer 2A and the bulk porosity of the uppermost crust. Bazin *et al.* (2001) report a highly variable layer 2A thickness in the vicinity of the 9°03′N OSC, with an average value of 430 m. The thickest layer 2A reported by these authors (800–900 m) was found in the southern half of the present OSC basin, in basin 1a, and beneath basin 1b (Fig. 1). Synthetic models (Appendix B) show that our experimental configuration resolves local thickening of layer 2A to 1 km beneath basin 3 (although the amplitude of the recovered anomaly is highly attenuated), and that the emplacement of an additional 600 m of low-velocity material on top of the crust is sufficient to explain the negative anomaly found along the outer western line near 9°10′N. Thus, if crustal accretion at the OSC ∼300 kyr ago was similar to the present-day processes taking place at the 9°03′N OSC, an anomalously thick extrusive layer of high-porosity lavas explains the low velocities beneath relict overlap basin 3.

While not required by our data, other factors such as tectonic alteration and fracture-induced porosity may contribute to the low-velocity anomaly, as suggested by the rotation of overlap basin 3 inferred from magnetic data (Carbotte & Macdonald 1992). The anomaly extends to ∼3 km below the seafloor, and a broader, lower-amplitude negative anomaly is present in the lower crust (Fig. 5e), consistent with the low seismic velocities in layer 3 in this same area reported by Christeson *et al.* (1997). Although some vertical smearing of a shallow anomaly in the tomography inversion may occur (Appendix B), the most likely source for the middle- and lower-crustal anomaly is porosity induced by shearing and/or alteration. Therefore, it is possible that hydrothermal circulation and alteration can extend deeply within the crust when the pathways for fluid flow are opened.

The western section of profile EPR-5 runs along the northern edge of the relict basins 3–5 (Fig. 1). All of these basins show negative

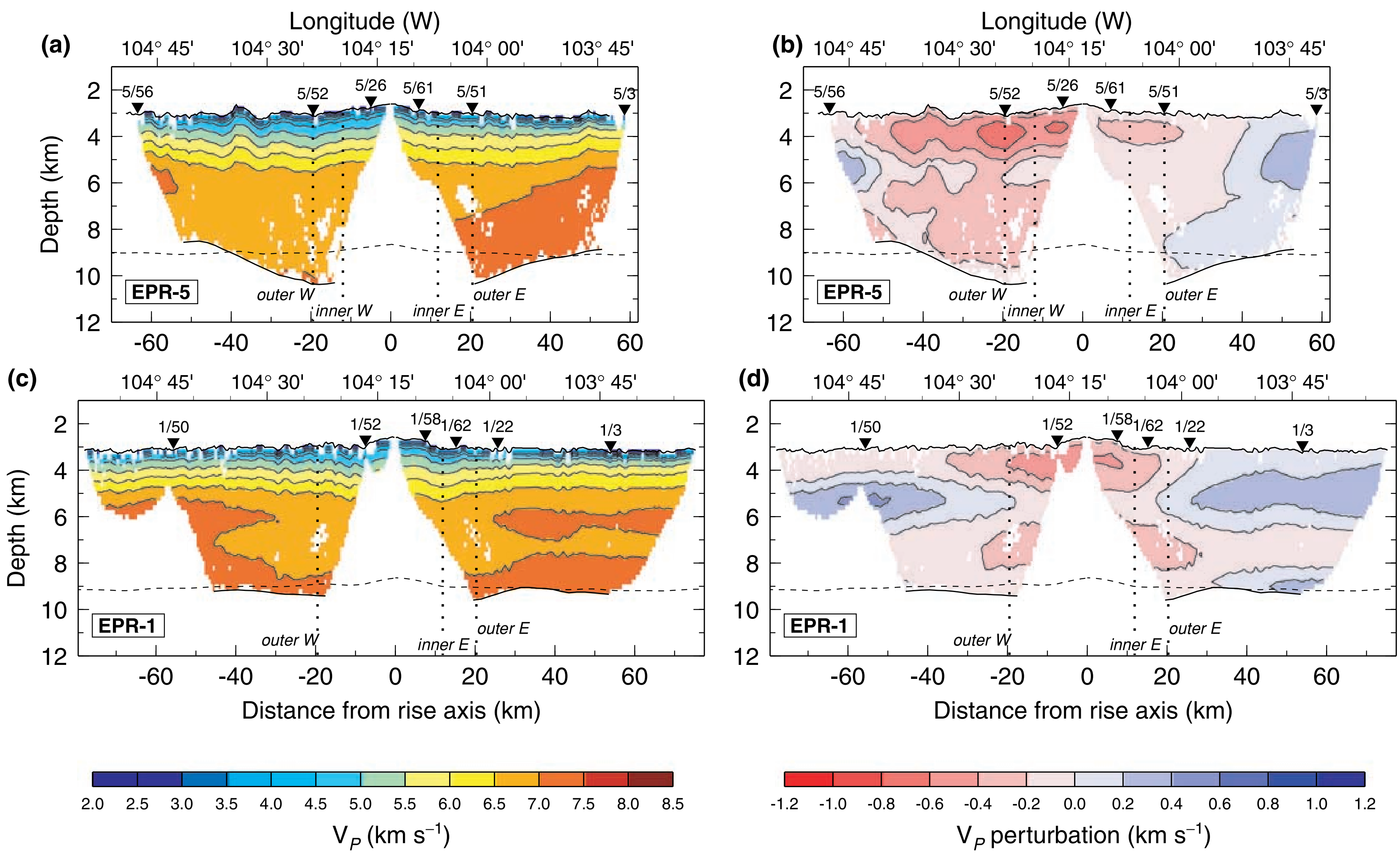

Figure 6. Final 2-D velocity models and velocity perturbations for profiles EPR-5 (a) and (b) and EPR-1 (c) and (d). Masking, contouring, and colour scales are as in Fig. 5. Dashed and solid lines are initial and final Moho depth. Vertical dotted lines show the crossing points with the axis-parallel profiles. Numbered triangles are the ocean-bottom instruments.

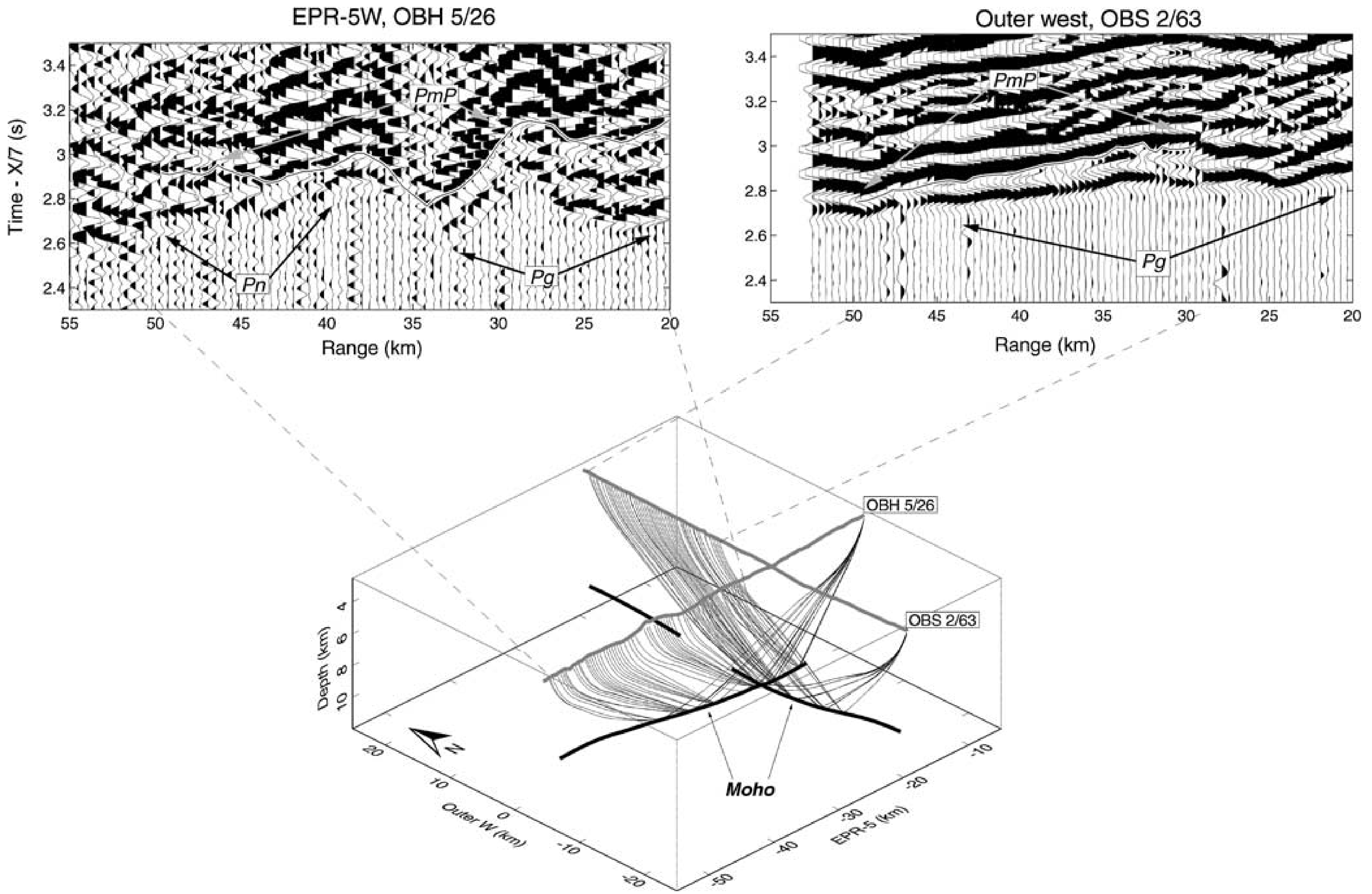

Figure 7. 3-D view of the rays sampling the thickest section of the crust west of the rise axis near 9°15′N for instruments OBH 5/26 and OBS 2/63. Top panels are the observed seismic record sections with the predicted *PmP* traveltimes for rays shown in the bottom diagram.

velocity anomalies (0.4–0.6 km s^{-1}) in the upper and middle crust, and a more moderate, broader negative anomaly in the lower crust. These findings support the above interpretation of the structure of basin 3, and provide additional evidence that reduced seismic velocities from the seafloor to Moho depths is a general characteristic of overlap basins. An exception is overlap basin 2 identified by Carbotte & Macdonald (1992) at ∼9°00′N , 104°25′W (Fig. 1). The outer western profile runs across this feature but our results do not show any significant crustal velocity anomaly beneath this basin (Fig. 5e). Bazin *et al.* (2001) suggest that the lack of reduced upper-crustal velocities in this basin might be related to formation after a northward jump of the OSC, in contrast to the other relict basins that were formed by southward propagation of the OSC (Carbotte & Macdonald 1992).

The southward propagation of the OSC has left a broad, diffuse discordant zone in the Cocos Plate (Carbotte & Macdonald 1992) that is characterized by moderately low upper- and middle-crustal seismic velocities, as observed along the eastern profiles between 9°00′N and 9°15′N (Figs 5g and h). As the eastern limb propagates into older crust, fracturing and alteration probably reduce crustal velocities within the discordant zone. We attribute the lack of reduced crustal velocities within the discordant zone along profile EPR-5, between 104°W and 103°45′W (Fig. 6b), to the large spacing between instruments 51 and 3.

6.1.2 Segment centre

Segment centres (between 9°20′N and 9°50′N along the northern segment, and between 8°35′N and 8°55′N along the southern segment) are characterized by mid-crustal seismic velocities that are relatively higher than at segment ends (Figs 4 and 5). The maximum velocity anomalies are found at ∼2 km subseafloor depth, probably within the sheeted dyke complex (e.g. Detrick *et al.* 1994). Thus, the high-velocity mid-crust along segment centres is probably the result of low-intensity tectonic alteration, and may be a larger ratio of intrusive dikes to extrusive lavas than at segment ends.

Along the outer western line, the positive anomaly near the centre of the northern segment is locally disrupted by an upper-crustal negative anomaly at 9°55′N beneath the Lamont Seamounts (Fig. 5e). Many Pacific seamounts (e.g. Hammer *et al.* 1994; Grevemeyer *et al.* 1998) are characterized by lower seismic velocities than the surrounding ocean crust, suggesting that small- and medium-size seamounts are built predominantly from a succession of extrusive layers.

6.1.3 Crustal anisotropy and age dependence of the velocity structure

A study of crustal anisotropy at the rise axis at 9°30′N found a 4 per cent anisotropy within the upper 1 km, 2 per cent from 1 to 2 km and 0 per cent below 2 km depth (Dunn & Toomey 2001). At the intersection of the axis-parallel and cross-axis lines, the velocities in the upper 0.5–2.0 km measured in the ridge-parallel direction are consistently faster (∼0.2–0.3 km s^{-1}) than those measured in the spreading direction (Fig. 8a). The differences gradually disappear between 2 and 4 km below the seafloor. This result is consistent with a 3–6 per cent seismically anisotropic upper crust (Fig. 8b) probably caused by cracks aligned perpendicular to the spreading direction.

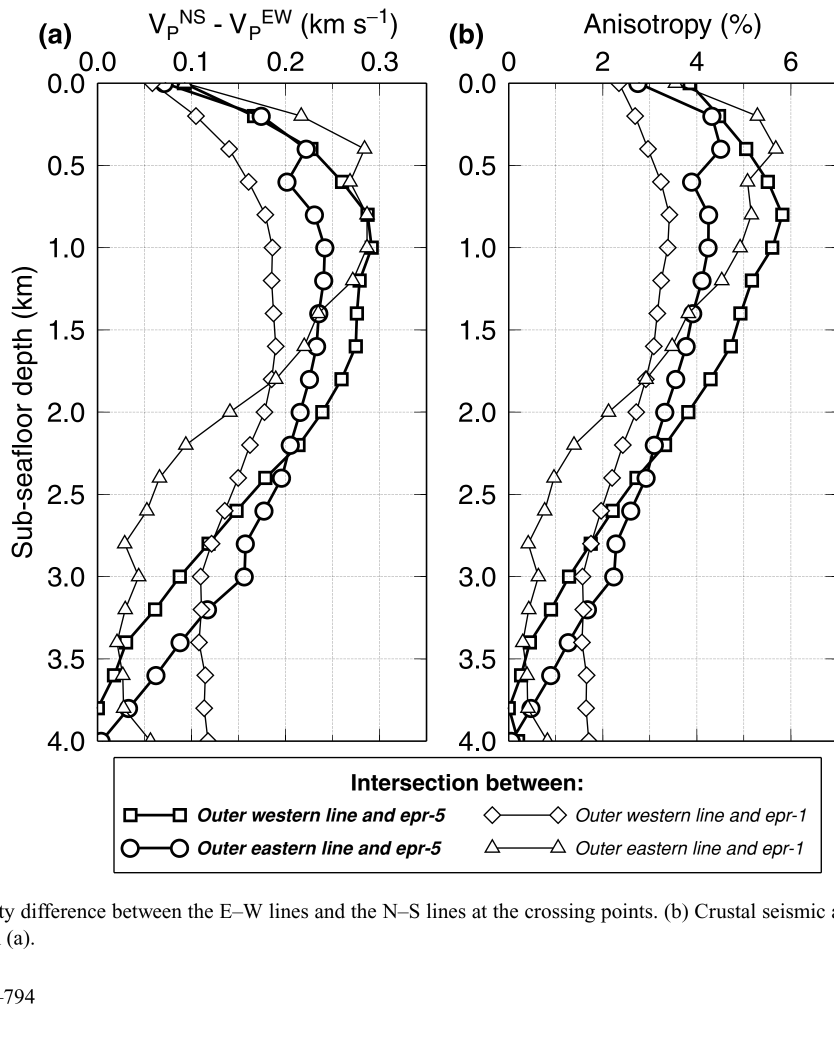

Figure 8. (a) Crustal velocity difference between the E–W lines and the N–S lines at the crossing points. (b) Crustal seismic anisotropy calculated from the velocity differences shown in (a).

The amplitude of the anisotropy found in our study is comparable to that of Dunn & Toomey (2001); the differences between both studies may be attributed to the different resolution scales.

Within the upper 1–4 km of the crust, velocities increase away from the ridge axis between 10 and 40–50 km off-axis (Fig. 6d). This is probably caused by temperature variations and hydrothermal alteration products sealing fractures and pores as the crust ages and cools, as observed in other areas of the Pacific basin (e.g. Houtz & Ewing 1976; Grevemeyer & Weigel 1997).

6.2 Crustal thickness variations

The results shown in Figs 5 and 6 display an intriguing pattern of crustal thickness variations. The profile on 300 kyr old crust on the Cocos Plate (Fig. 5d) shows the simplest variation—a gradual thickening of the crust away from both the Clipperton and Siqueiros FZs with the thickest crust located midway between these offsets. On the younger axis-parallel profile on this same plate (Fig. 5c) the crust also thickens southward away from the Clipperton FZ, but the thickest crust is found further south between the 9°03′N OSC and the Siqueiros FZ. The axis-parallel profile on 300 kyr old seafloor on the Pacific Plate (Fig. 5a) shows thicker than normal crust beneath the Lamont seamounts and approximately midway between the Clipperton and Siqueiros FZ, just north of a relict overlap basin that marks the off-axis trace of the 9°03′N OSC. The cross-axis profile at this same latitude, just north of the OSC, shows a pronounced thickening of the crust towards the rise axis (EPR-5; Fig. 6a). However, the refraction line across the centre of the southern segment at 8°40′N does not show such pronounced crustal thickening towards the rise axis (EPR-1 Fig. 6c).

In order to visualize and interpret this pattern of crustal thickness variations, we have interpolated the measurements along the six profiles on to a crustal thickness map (Fig. 9). The mean crustal thickness along the EPR between the Siqueiros and Clipperton fracture zones is 6.7–6.8 km. The thickest crust is found beneath the Lamont seamounts ($\sim$ 9 km), and in a southward-pointing band located just north of the off-axis trace of the 9°03′N OSC (7.3–7.8 km). The thinnest crust (< 6 km) is found proximal to the Clipperton and Siqueiros FZ. The crust associated with the off-axis trace of the 9°03′N OSC is not anomalously thin if compared with the average crustal thickness of the northern and southern segments. This is consistent with recent studies showing that magma supply beneath this axial discontinuity is not significantly different from segment centres (Kent *et al.* 2000; Dunn *et al.* 2001). Our results are thus not consistent with the view that OSCs form over regions of reduced magma supply (Macdonald *et al.* 1988).

The observed variations in crustal thickness in this area could be related to temporal and/or spatial variations in magma supply. However, the band of thick crust located just north of the off-axis wake of the at 9°03′N OSC mapped by Carbotte & Macdonald (1992) suggests a close genetic link between this thickened crust and the evolution of this OSC over the past 0.5 Myr. Therefore, the interpretation of segment-scale crustal thickness variations should take into account the kinematics of propagating axial discontinuities, and the time a crustal column is exposed to the melt supply system. These mechanisms will be discussed in Section 6.2.4.

6.2.1 *Comparison with MCS-derived crustal thickness measurements*

We found a similar pattern in crustal thickness variation to that determined by Barth & Mutter (1996) using MCS reflection data, with a gradual thickening of the crust from north to south along the northern ridge segment, and the location of the thickest crust just north of the 9°03′N OSC. However, the magnitude of the crustal thickness variation we observe along the northern ridge segment between 9°50′N and 9°15′N ($\sim$1.3–1.8 km excluding the Lamont seamounts)

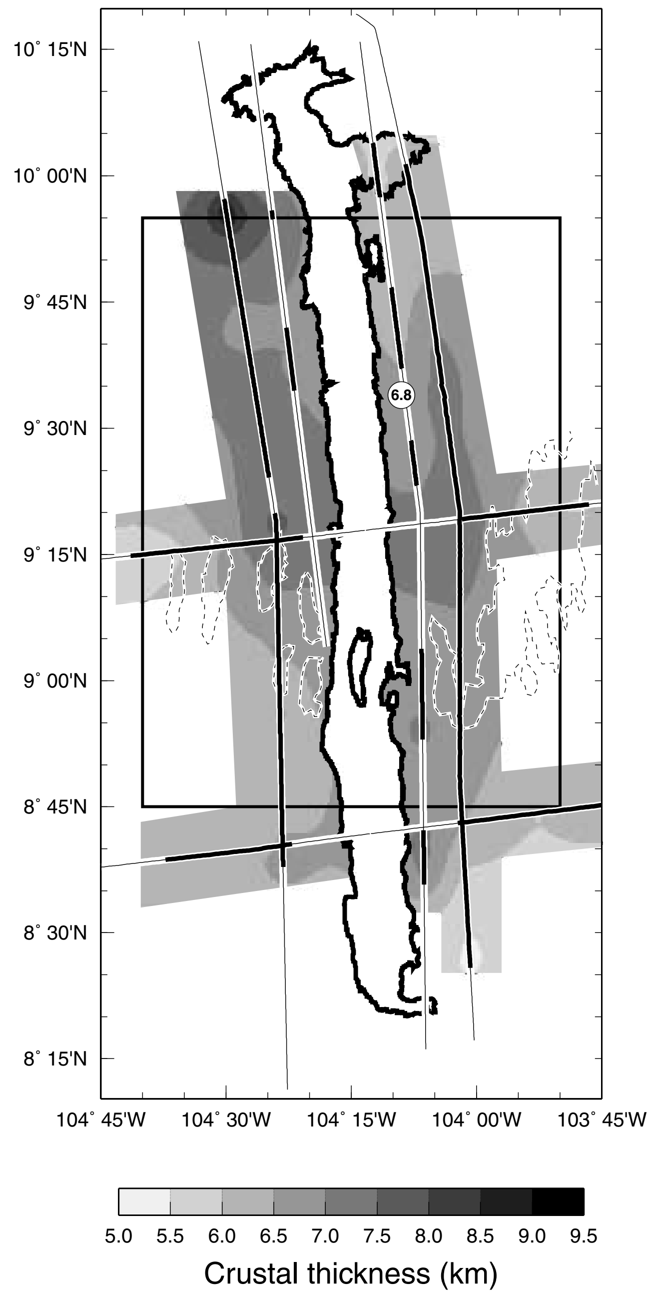

Figure 9. Contour map of the crustal thickness in the study area. The crustal thickness measurements along the sections of the profiles with *PmP* reflections (thick solid lines) were interpolated on to a grid as a harmonic surface (no maxima or minima are possible except at the data points) using a continuous curvature algorithm (Smith & Wessel 1990). The map is masked where no data points are available. Contours shown every 0.5 km. Dashed lines show the wake of the propagating OSC as in Fig. 1. Circled number is the crustal thickness (in km) reported by Vera *et al.* (1990) at that location. The box corresponds to the study area of Barth & Mutter (1996) shown in Fig. 2, for comparison. Thin black lines are the seismic profiles. The 2800 m water depth isolines around the rise axis and 9°03′N overlap basin are shown for reference purposes (see Fig. 1).

is significantly less than the ∼2.3 km of variation reported in their study. In particular, crustal thickness along the northern ridge segment between 9°30′N and 9°50′N estimated from MCS reflection data is relatively thin (5–6 km), compared with the ∼6.2–6.7 km thick crust found in our study. Our results are also more consistent with the value of 6.8 km estimated by Vera *et al.* (1990) at ESP-1 east of the ridge axis near 9°32′N (Fig. 9). The MCS and wide-angle-derived crustal thickness estimates are in closer agreement north of the OSC between 9°07′N and 9°25′N where both data sets indicate >7 km thick crust is present.

There are several possible explanations for these differences in estimated crustal thickness. First, it should be noted that both data sets do not sample exactly the same area. The MCS data mapped Moho TWTT between 8°50′N and 9°50′N in crust generally less than 200 kyr old (Fig. 2). Our refraction and wide-angle reflection data encompass a wider latitude range and are primarily constrained by axis-parallel lines located on older, 300 kyr old crust (Fig. 9). MCS data measure TWTT to Moho that is affected by both crustal thickness and velocity variations. Barth & Mutter (1996) argued that the crustal thickness can be inferred from crustal reflection traveltimes even in cases where the crustal velocity structure is unknown because there is a linear relationship between the crustal TWTT and the crustal thickness (inferred from the global compilation of White *et al.* 1992). We have tested this relation using our refraction results (Fig. 10) and find that it is valid, except where crustal velocities are unusually low, such as beneath relict OSC basins or near fracture zones. In these areas the MCS-derived estimates will overestimate the crustal thickness. However, this cannot explain why MCS-derived crustal thicknesses north of 9°30′N are significantly below those determined from wide-angle data.

One possible source for the difference is that at near-vertical incidence MCS reflection and wide-angle reflection data sample the Moho in different ways. Wide-angle *PmP* arrivals are from rays turning within the high-velocity gradient Moho transition zone and the crustal thickness measured from wide angle data may thus correspond to the depth of the mid-point or base of the Moho transition zone. In contrast, the near-vertical incidence Moho reflections observed in MCS data are more likely to represent the top of the Moho transition zone (e.g. Barth & Mutter 1996). We note that the linear fit to our crustal two-way traveltime crustal thickness pairs (Fig. 10) more closely matches the linear trend found by Barth & Mutter (1996) when the crustal thickness is defined as the depth to the 8 km s^{-1} velocity (dashed line) than as the depth to the top of the transition zone (thin solid line).

A second possible source for these differences is the difficulty in identifying Moho reflections on some MCS record sections and of accurately measuring the onset time of second-arriving *PmP* phases in wide-angle data. The onset of the secondary *PmP* arrival can be masked by the coda of the first arrivals. Thus it is possible that our *PmP* picks are somewhat late with respect to the onset of the *PmP* phase, which could lead to an overestimation of crustal thickness. However, as illustrated in Appendix A (Figs A4–A7), *PmP* picking

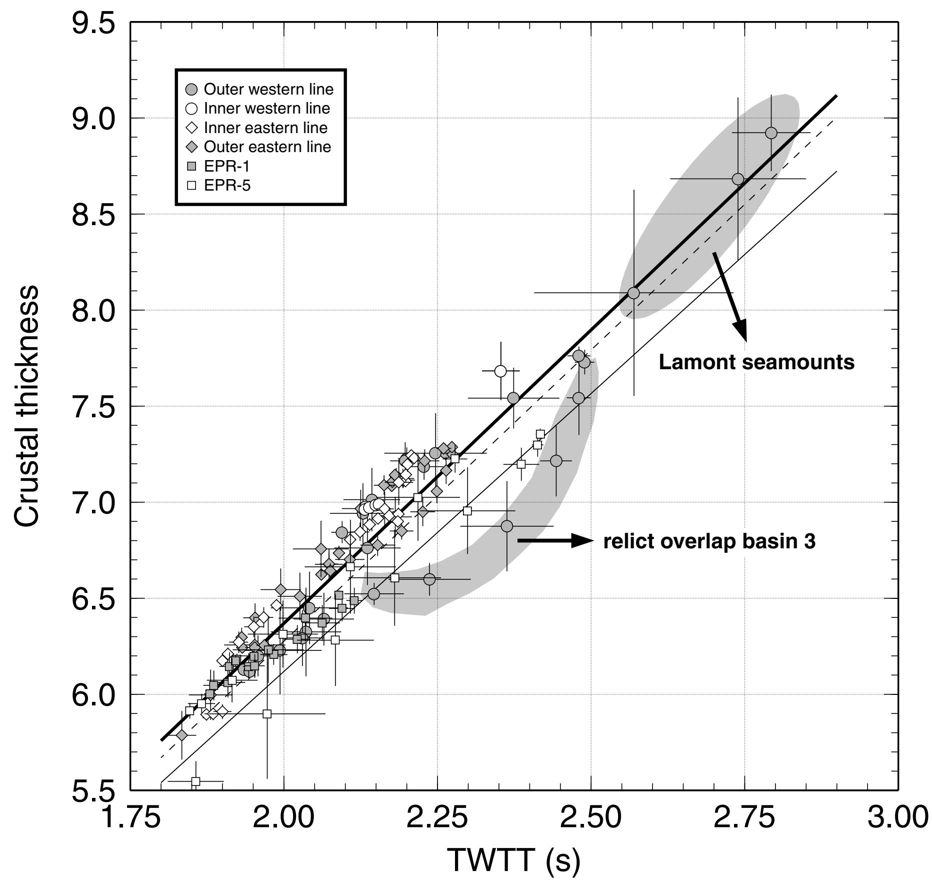

Figure 10. Crustal thickness versus crustal TWTT. Symbols are values obtained in this study, averaged over 10 km wide bins. Error bars are standard deviations. Shaded areas show the data corresponding to the relict overlap basin 3 and the Lamont seamounts. The thick solid line is the best-fitting linear regression of the data points, excluding the anomalous values of the relict overlap basin (y [km] = $3.054x$ [s] + 0.261). Thin solid and dashed lines are the global linear regressions from Barth & Mutter (1996) for the crustal thickness measured as the top of the Moho transition zone and as the depth to 8 km s^{-1}, respectively.

errors would have to be $>$50–60 ms at 40 km shot–receiver range to explain the $>$1 km difference in crustal thickness along the northern ridge segment between MCS and wide-angle data, which seems unlikely. While late picking of *PmP* arrivals could introduce a bias in crustal thickness estimates it should not change our estimates of relative crustal thickness variation. We note that the best agreement between the MCS and wide-angle crustal thickness estimates is between 9°05′N and 9°30′N where a high-amplitude, impulsive Moho reflector is present in reflection sections. North of 9°30′N, where the largest discrepancy in crustal thickness estimates occurs, the Moho becomes weaker and sometimes discontinuous in the MCS data (see fig. 5 in Barth & Mutter 1996). We believe that the difficulty of picking Moho in reflection data north of 9°30′N and possible along-strike changes in the nature and thickness of the Moho transition zone in this area, are the most likely explanations for the different crustal thicknesses derived from MCS and wide-angle data along the northern ridge segment.

6.2.2 Explanation of small along-axis MBA anomalies

While we find less variation in crustal thickness in this area than previously reported, the along-axis variation we do see is still more than would be expected from the small along-axis MBA gradients found in this area (Madsen *et al.* 1990; Wang *et al.* 1996). The explanation for this lack of a gravity signature associated with seismically determined crustal thickness variations is not clear. In order to mask crustal thickness variations in the MBA, crustal or mantle densities would have to be anticorrelated with crustal thickness, i.e. areas of thick crust would have to be associated with anomalously high crustal or mantle densities and/or vice versa.

Crustal density effects can be important near fracture zones—for example, anomalously low crustal densities in the Clipperton and Siqueiros FZs partially mask the gravity signature of the thinner crust present in these areas in the MBA. We have considered whether variations in crustal thickness away from these fracture zones (e.g. the southward increase in crustal thickness between 9°50′N and 9°10′N) could also be masked in the MBA by density variations, especially in the lower crust (e.g. an increase in lower-crustal density from north to south). Lower-crustal gabbros drilled in Hole 735B at Atlantis Bank show a bi-modal distribution of elastic properties (Iturrino *et al.* 1991). Olivine gabbros have an average $V_p = 7.1$ km s^{-1} and a density of 2.95 g cm^{-3}, while oxide gabbros enriched in iron–titanium (Fe–Ti) have lower seismic velocities (6.75 km s^{-1}) and higher densities (3.22 g cm^{-3}). On-bottom gravity measurements on a massive exposure of oxide gabbro near Hole 735B suggest densities even higher than mantle peridotites (Matsumoto *et al.* 2001). Thus compositional variations in the lower crust can be accompanied by significant lower-crustal density variations. Along our two best-constrained profiles (Figs 5e and h), thicker crust is associated with somewhat lower velocities in the lower crust and possibly higher density if enriched in Fe–Ti. However, this pattern is not systematic along the profiles and some uncertainty exists in lower-crustal velocities caused by the inherent trade-off between crustal thickness and lower-crustal velocity when modelling wide-angle reflection data (Appendix B). Fe–Ti enrichment forming high-density oxide gabbros also requires high degrees of crystal–liquid fractionation in the crust, and melt flow in the crust away from the melt supply centre (Dick *et al.* 2000). Segment-scale redistribution of melt within the crust along this portion of the EPR is, however, inconsistent with the correlation of fine-scale variations in crustal magma chamber properties, axial morphology, petrologic segmentation and hydrothermal activity noted by Dunn *et al.* (2000). Thus a strong case cannot be made that lower-crustal density variations explain the small along-axis MBA gradients observed in this area. An alternative explanation is that there is a systematic south to north increase in the Moho transition zone thickness (Barth & Mutter 1996), and/or a decrease in mantle density between 9°10′N and 9°50′N (Wang *et al.* 1996). Additional data and analysis will be required to see whether mantle density variations offer an explanation for the puzzling lack of correlation between seismically determined crustal thickness variations and MBA in this area.

6.2.3 Relationship between the crustal velocity and the thickness variations, tectonic segmentation and spreading rate

Our results provide insight into the relationship between crustal velocity and thickness variations, tectonic segmentation and spreading rate. Figs 11(a) and (b) show that along the EPR between the Clipperton and Siqueiros FZs tectonic segmentation correlates well with the average crustal velocity. Crustal velocities are reduced near fracture zones and near OSC discontinuities. The crustal thickness, in contrast, is not well correlated with tectonic segmentation. As we will discuss in Section 6.2.4, this may be related to the kinematic evolution of the 9°03′N OSC and thus may not be a general feature of fast spreading ridges. In this area, excluding anomalous features such as seamounts, we have found approximately 2–2.5 km of crustal thickness variation between the thickest crust found just north of the 9°03′N OSC (7.3–7.8 km) and the thinnest crust within the Siqueiros transform (5.3 km). This is much more crustal thickness variation than is commonly believed to exist at the segment scale at fast spreading ridges, and indicates that it is incorrect to assume that crust formed at fast spreading rates is of uniform thickness. In comparison, a study of the slow spreading MAR (Canales *et al.* 2000) shows that both the crustal velocity and the thickness are strongly correlated with ridge segmentation. The largest crustal thickness corresponds to segment centres, while ridge discontinuities are associated with anomalously thin, low-velocity crust. A single slow spreading ridge segment can display more than 4 km of crustal thickness variation (Fig. 11c), encompassing the entire variation observed along the global mid-ocean ridge system (White *et al.* 1992). Thus, while larger than expected, the magnitude of the crustal thickness variation at the EPR in the 9°N region is still approximately half that observed at slower spreading ridges, supporting the hypothesis that there are fundamental differences between slow and fast spreading ridges in how melt is supplied from the mantle to the crust and how the magmatic crust is constructed.

6.2.4 Implications for mantle flow beneath fast spreading ridges and the role of OSCs in patterns of crustal thickness variation

Wang *et al.* (1996) proposed the presence of a low-density, melt-rich mantle diapir beneath the EPR at ∼9°50 in order to explain the lack of a significant gravity signature associated with the crustal thickening from north to south along the northern segment reported by Barth & Mutter (1996). While we find a similar pattern of crustal thickening along the northern ridge segment, the change in crustal thickness we observe is slightly more than half that determined by Barth & Mutter (1996). We also do not find anomalously thin crust near 9°50′N; instead, the crust here has a thickness close to the mean crustal thickness for this area. Thus the mass anomaly required to explain the lack of a significant MBA anomaly in this area is significantly less than that calculated by Wang *et al.* (1996),

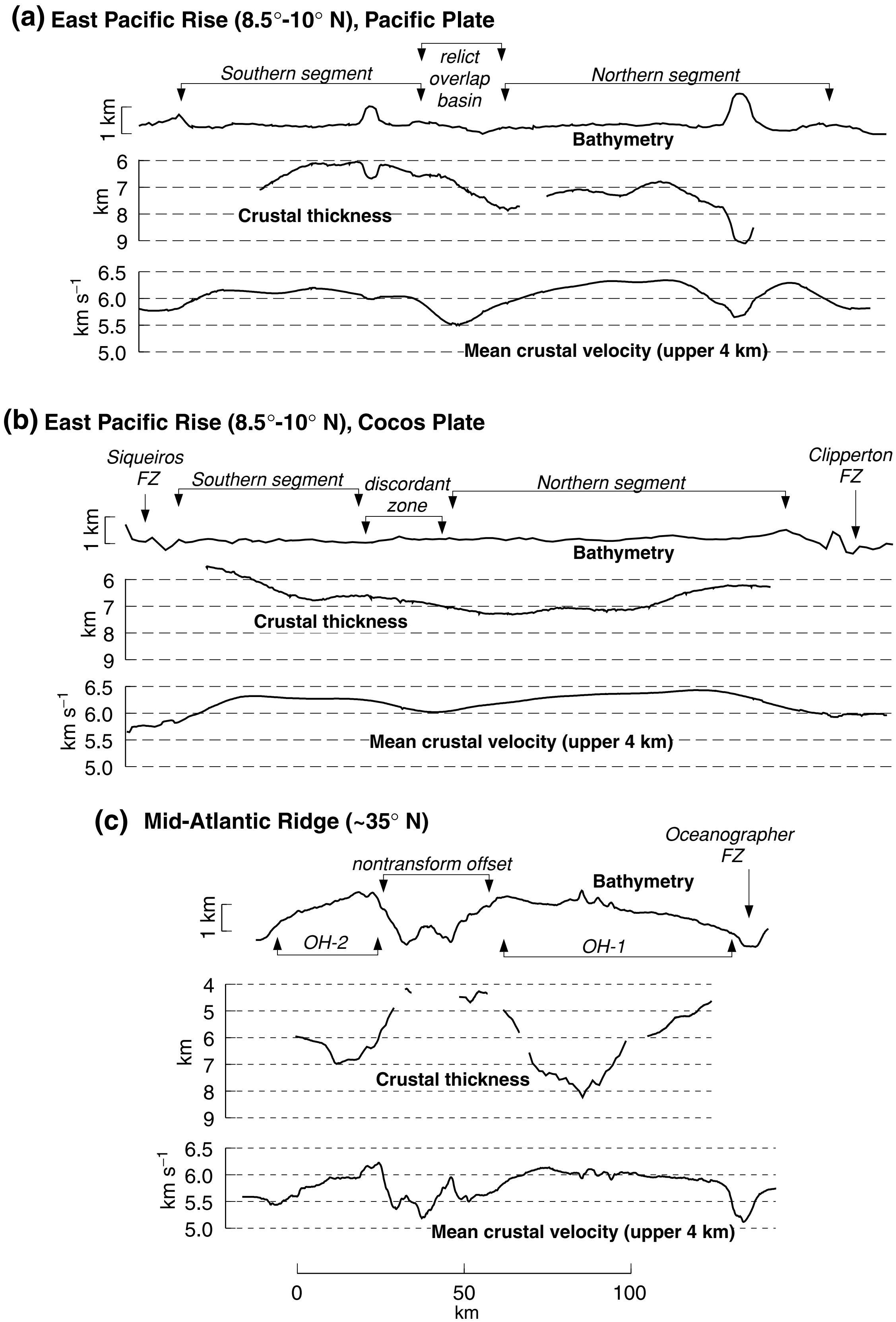

Figure 11. Comparison of segmentation and crustal structure between the fast spreading EPR and the slow spreading MAR. Segmentation, crustal thickness and mean crustal seismic velocity variations along: (a) the EPR between 8°30′N and 10° N in the Pacific Plate, (b) in the Cocos Plate and (c) MAR south of the Oceanographer FZ (segments OH-1 and OH-2, results from Canales *et al.* 2000).

weakening the evidence for a mantle diapir beneath the EPR at ∼9°50′N.

The southward-pointing band of thick crust that we observe north of 9°10′N also seems inconsistent with a single, large mantle diapir centred at 9°50′N. Assuming the diapir is fixed relative to the spreading geometry it should have left a wake of thin and thick crust parallel to the spreading direction, which is not observed. A V-shaped wake of thick crust similar to our observation could result from both, lower-crustal flow away from the diapir as proposed by Barth & Mutter (1996), and propagation of the OSC, but only if the OSC is a barrier to along-axis flow. However, the evidence for crustal melt bodies within the OSC (Kent *et al.* 2000), and the continuity of a subcrustal low-velocity zone beneath the OSC (Dunn *et al.* 2001), seems to argue against the idea that the OSC represents a thermal or mechanical boundary to along-axis lower-crustal flow.

The locus of thickened crust immediately to the north of the wake of the southward-propagating OSC suggests a possible genetic relationship between the OSC and the thickened crust. It also coincides with an asymmetric distribution of melt in the crust and upper mantle with respect to the spreading axis immediately north of the 9°03′N OSC (Kent *et al.* 1993b, 2000; Dunn *et al.* 2001; Crawford & Webb 2002) possibly caused by a change in the spreading direction ∼1 Ma (Carbotte & Macdonald 1992). Propagation of an OSC can transfer a young crustal unit above the mantle melt source from one plate to the conjugate one, locally increasing the thickness of the crustal unit. If the migration of the offset reverses direction, as proposed for the 9°03′N OSC at 0.24 Ma Carbotte & Macdonald (1992), the crustal unit can pass over the melt source more than once. The area of crust exposed to this thickening mechanism and the magnitude of the thickening would be controlled by the length of the offset, the propagation velocity and by the width of the mantle melt source (16 km in the study area, Dunn *et al.* 2001). In addition, as the OSC accommodates the spreading geometry, the crust in the vicinity of the overlap basin could be temporarily stagnated, increasing its residence time over the melt source. Subsequent propagation of the offset would leave a track of thickened crust behind the wake of the OSC, although it is unclear why the thickened crust is not observed directly beneath the discordant zone. Thus the crustal thickening from north to south along the northern segment could be attributed to the kinematics of a southward-propagating OSC without invoking along-axis migration of melt away from a mantle diapir at 9°50′N.

7 CONCLUSIONS

The main conclusions of this study of EPR crustal structure between the Clipperton and Siqueiros fracture zones are as follows.

(1) There is a strong correlation between ridge segmentation and upper- and mid-crustal seismic velocities. Segment discontinuities such as the Siqueiros and Clipperton FZs, and the off-axis trace of the 9°03′N OSC, have low seismic velocities relative to a 1-D reference model, while segment centres have relatively high crustal *P*-wave velocities.

(2) The reduced crustal velocities at FZs are most likely to be caused by extensive fracturing and brittle deformation in the transform domain. A pronounced negative crustal velocity anomaly beneath a relict overlap basin left on the Pacific Plate by the southward-propagating 9°03′N OSC is consistent with the presence of an unusually thick extrusive section in the basin owing to pooling of high-porosity lavas in the basin from the nearby OSC limbs, and with shearing and alteration of the crust beneath the basin. The discordant zone left by the OSC on the Cocos Plate is characterized by moderately low crustal velocities probably caused by crustal fracturing as the OSC propagated into older crust.

(3) Higher upper- and mid-crustal velocities near segment centres in the 9° N region may reflect a higher ratio of dikes to extrusives, and lower-intensity tectonic alteration of the crust, than near segment ends.

(4) Excluding anomalous features such as seamounts, we have found a total range of crustal thickness variation of 2–2.5 km in the 9° N region with the thickest crust located just north of the 9°03′N OSC (7.3–7.8 km) and the thinnest crust found within the Siqueiros transform (5.3 km). This is much more crustal thickness variation than is commonly believed to exist at the segment scale at fast spreading ridges, and indicates that it is incorrect to assume that crust formed at fast spreading rates is of uniform thickness.

(5) Along the northern ridge segment between 9°50′N and 9°15′N crustal thickness variations (1.3–1.8 km) are significantly less than the ∼2.3 km previously inferred from MCS data. Thus mantle density variations previously invoked to explain the small along-axis MBA gradients along this segment may not be as large as inferred from MCS-derived crustal thickness data, weakening the evidence for a low-density, melt-rich, mantle diapir at ∼9°50′N.

(6) Crust associated with the off-axis trace of the 9°03′N OSC is not anomalously thin and is thus not consistent with the view that OSCs form over regions of reduced magma supply from the mantle.

(7) The southward migration of the OSC has been accompanied by crustal thickening immediately to the north of the OSC, leaving an off-axis band of thickened crust behind the wake of the OSC. We propose that as the OSC propagates, young crust is transferred from one plate to the conjugate one—and/or temporarily stagnated—over the mantle magma source, and new material is added to the crust. Thus crustal thickness variation along the northern segment can be attributed to the evolution of the 9°03′N OSC without invoking a single, large mantle diapir at 9°50′N as previously proposed.

ACKNOWLEDGMENTS

We thank Captain Ian Young, Science Officer Chris Liedhold and the crew of the R/V *Maurice Ewing* Leg 97-08 for the data acquisition. We are grateful to the WHOI OBS group, namely, Jim Dolan, Dave DuBois, John Hallinan, Rob Handy and Beecher Wooding, and the SIO technician Russell Johnson for their technical support. We thank Jun Korenaga for making available his tomography code and for helping us with its use. We also thank Rob Dunn, John Sinton and Henry Dick for helpful discussions. Comments by two anonymous reviewers helped to improve the original manuscript. The GMT software package (Wessel & Smith 1995) was used in the preparation of this paper. This work was supported by the National Science Foundation grant OCE-9634132 to the Woods Hole Oceanographic Institution, OCE-9633264 to the University of Oregon and OCE-9633814 to the University of Washington. Woods Hole Oceanographic Institution contribution 10825.

REFERENCES

Barth, G.A. & Mutter, J.C., 1996. Variability in oceanic crustal thickness and structure: multichannel seismic reflection results from the northern East Pacific Rise, *J. geophys. Res.,* **101,** 17 951–17 975.

Batiza, R. & Niu, Y., 1992. Petrology and magma chamber processes at the East Pacific Rise ∼9°30′N, *J. geophys. Res.,* **97,** 6779–6797.

Bazin, S., van Avendok, H.J.A., Harding, A.J., Orcutt, J.A., Canales, J.P. & Detrick, R.S., 1998. Crustal structure of the flanks of the East Pacific Rise: implications for overlapping spreading centers, *Geophys. Res. Lett.,* **25,** 2213–2216.

Bazin, S. *et al.*, 2001. Three-dimensional shallow crustal emplacement at the 9°30′N overlapping spreading center on the East Pacific Rise: correlations between magnetization and tomographic images, *J. geophys. Res.,* **106,** 16 101–16 117.

Begnaud, M.L., McClain, J.S., Barth, G.A., Orcutt, J.A. & Harding, A.J., 1997. Velocity structure from forward modeling of the eastern ridge-transform intersection area of the Clipperton Fracture Zone, East Pacific Rise, *J. geophys. Res.,* **102,** 7803–7820.

Bell, R.E. & Buck, W.R., 1992. Crustal control of ridge segmentation inferred from observations of the Reykjanes Ridge, *Nature,* **357,** 583–586.

Canales, J.P., Detrick, R.S., Bazin, S., Harding, A.J. & Orcutt, J.A., 1998. Off-axis crustal thickness across and along the East Pacific Rise within the MELT area, *Science,* **280,** 1218–1221.

Canales, J.P., Detrick, R.S., Lin, J., Collins, J.A. & Toomey, D.R., 2000. Crustal and upper mantle seismic structure beneath the rift mountains and across a nontransform offset at the Mid-Atlantic Ridge (35°N), *J. geophys. Res.,* **105,** 2699–2719.

Carbotte, S.M. & Macdonald, K.C., 1992. East Pacific Rise 8°–10°30′N: evolution of ridge segment and discontinuities from SeaMARC II and three-dimensional magnetic studies, *J. geophys. Res.,* **97,** 6959–6982.

Christeson, G.L., Purdy, G.M. & Fryer, G.J., 1994. Seismic constraints on shallow crustal emplacement processes at the fast spreading East Pacific Rise, *J. geophys. Res.,* **99,** 17 957–17 973.

Christeson, G.L., Shaw, P.R. & Garmany, J.D., 1997. Shear and compressional wave structure of the East Pacific Rise, 9°–10°N, *J. geophys. Res.*, **102,** 7821–7835.

Crawford, W.C. & Webb, S.C., 2002. Variations in the distribution of magma in the lower crust and at the Moho beneath the East Pacific Rise at 9°–10°N, *Earth planet, Sci. Lett.,* **203,** 117–130.

Creager, K.C. & Dorman, L.M., 1982. Location of instruments on the seafloor by joint adjustment of instrument and ship position, *J. geophys. Res.,* **87,** 8379–8388.

DeMets, C., Gordon, R.G., Argus, D.F. & Stein, S., 1990. Current plate motions, *Geophys. J. Int.,* **101,** 425–478.

Detrick, R.S., Buhl, P., Vera, E.E., Mutter, J.C., Orcutt, J.A., Madsen, J.A. & Brocher, T.M., 1987. Multi-channel seismic imaging of a crustal magma chamber along the East Pacific Rise, *Nature,* **326,** 35–41.

Detrick, R.S., Collins, J.A., Stephen, R.A. & Swift, S.A., 1994. *In situ* evidence for the nature of the seismic layer 2/3 boundary in oceanic crust, *Nature,* **370,** 288–290.

Detrick, R.S., Needham, H.D. & Renard, V., 1995. Gravity anomalies and crustal thickness variations along the Mid-Atlantic Ridge between 33°N and 40°N, *J. geophys. Res.,* **100,** 3767–3787.

Dick, H.J.B. *et al.*, 2000. A long, in situ section of the lower ocean crust: results of ODP Leg 176 drilling at the Southwest Indian ridge, *Earth planet, Sci. Lett.,* **179,** 31–51.

Dunn, R.A. & Toomey, D.R., 1997. Seismological evidence for the three-dimensional melt migration beneath the East Pacific Rise, *Nature,* **388,** 259–262.

Dunn, R.A. & Toomey, D.R., 2001. Crack-induced seismic anisotropy in the oceanic crust across the East Pacific Rise (9°30′N), **189,** 9–17.

Dunn, R.A., Toomey, D.R. & Solomon, S.C., 2000. Three-dimensional seismic structure and physical properties of the crust and shallow mantle beneath the East Pacific Rise at 9°30′N, *J. geophys. Res.,* **105,** 23 463–23 478.

Dunn, R.A., Toomey, D.R., Detrick, R.S. & Wilcock, W.S.D., 2001. Continuous mantle melt supply beneath an overlapping spreading center on the East Pacific Rise, *Science,* **291,** 1955–1958.

Fornari, D.J., Ryan, W.B.F. & Fox, P.J., 1984. The evolution of craters and calderas of young seamounts: insights from Sea MARC I and Sea Beam sonar surveys of a small seamount group near the axis of the East Pacific Rise at ∼10°N, *J. geophys. Res.,* **89,** 11 069–11 083.

Forsyth, D.W., 1992. Geophysical constraints on mantle flow and melt migration beneath mid-ocean ridges, in *Mantle Flow and Melt Generation at Mid-ocean Ridges,* Vol. 71, pp. 1–65, eds Phipps Morgan, J., *et al.*, AGU, Washington, DC.

Grevemeyer, I. & Weigel, W., 1997. Increase of seismic velocities in upper oceanic crust: the 'superfast' spreading East Pacific Rise at 14°14′S, *Geophys. Res. Lett.,* **24,** 217–220.

Grevemeyer, I., Weigel, W. & Jennrich, C., 1998. Structure and ageing of oceanic crust at 14°S on the East Pacific Rise, *Geophys. J. Int.,* **135,** 573–584.

Gripp, A.E. & Gordon, R.G., 1990. Current plate velocities relative to the hotspots incorporating the NUVEL-1 global plate motion model, *Geophys. Res. Lett.,* **17,** 1109–1112.

Hammer, P.T.C., Dorman, L.M., Hildebrand, J.A. & Cornuelle, B.D., 1994. Jasper Seamount structure: seafloor seismic refraction tomography, *J. geophys. Res.,* **99,** 6731–6752.

Harding, A.J., Kent, G.M. & Orcutt, J.A., 1993. A multichannel seismic investigation of upper crustal structure at 9°N on the East Pacific Rise: implications for crustal accretion, *J. geophys. Res.,* **98,** 13 925–13 944.

Haymon, R.M., Fornari, D.J., Edwards, M.H., Carbotte, S.M., Wright, D.J. & Macdonald, K.C., 1991. Hydrothermal vent distribution along the East Pacific Rise crest (9°09′–54′N) and its relationship to magmatic and tectonic processes on fast-spreading mid-ocean ridges, *Earth planet, Sci. Lett.,* **104,** 513–534.

Herron, T.J., Stoffa, P.L. & Buhl, P., 1980. Magma chamber and mantle reflections—East Pacific Rise, *Geophys. Res. Lett.,* **7,** 989–992.

Hooft, E.E.E., Detrick, R.S., Toomey, D.R., Collins, J.A. & Lin, J., 2000. Crustal and upper mantle structure along three contrasting spreading segments of the Mid-Atlantic Ridge, 33.5°–35°N, *J. geophys. Res.,* **105,** 8205–8226.

Houtz, R.E. & Ewing, J., 1976. Upper crustal structure as a function of plate age, *J. geophys. Res.,* **81,** 2490–2498.

Iturrino, G.J., Christensen, N.I., Kirby, S. & Salisbury, M.H., 1991. Seismic velocities and elastic properties of oceanic gabbroic rocks from Hole 735B, *Proc. Ocean Drill. Program Sci. Results,* **118,** 227–244.

Kent, G.M., Harding, A.J. & Orcutt, J.A., 1993a. Distribution of magma beneath the East Pacific Rise between the Clipperton transform and the 9°17′N deval from forward modeling of common depth point data, *J. geophys. Res.,* **98,** 13 945–13 969.

Kent, G.M., Harding, A.J. & Orcutt, J.A., 1993b. Distribution of magma beneath the East Pacific Rise near the 9°03′N overlapping spreading center from forward modeling of common depth point data, *J. geophys. Res.,* **98,** 13 971–13 995.

Kent, G.M. *et al.*, 2000. Evidence from three-dimensional seismic reflectivity images for enhanced melt supply beneath mid-ocean-ridge discontinuities, *Nature,* **406,** 614–618.

Klitgord, K.D. & Mammerickx, J., 1982. Northern East Pacific Rise: magnetic anomaly and bathymetric framework, *J. geophys. Res.,* **87,** 6725–6750.

Korenaga, J., Holbrook, W.S., Kent, G.M., Kelemen, P.B., Detrick, R.S., Larsen, H.-C., Hopper, J.R. & Dahl-Jensen, T., 2000. Crustal structure of the southeast Greenland margin from joint refraction and reflection seismic tomography, *J. geophys. Res.,* **105,** 21 591–21 614.

Lin, J. & Phipps Morgan, J., 1992. The spreading rate dependence of three-dimensional mid-ocean ridge gravity structure, *Geophys. Res. Lett.,* **19,** 13–16.

Lin, J., Purdy, G.M., Schouten, H., Sempéré, J.-C. & Zervas, C., 1990. Evidence from gravity data for focused magmatic accretion along the Mid-Atlantic Ridge, *Nature,* **344,** 627–632.

Lonsdale, P., 1989. The rise flank trails left by migrating offsets of the Equatorial East Pacific Rise axis, *J. geophys. Res.,* **94,** 713–743.

Macdonald, K.C. & Fox, P.J., 1983. Overlapping spreading centers: a new kind of accretionary geometry on the East Pacific Rise, *Nature,* **302,** 55–58.

Macdonald, K.C. & Fox, P.J., 1988. The axial summit graben and cross-sectional shape of the East Pacific Rise as indicators of axial magma chambers and recent volcanic eruptions, *Earth planet, Sci. Lett.,* **88,** 119–131.

Macdonald, K.C. *et al.*, 1988. A new view of the mid-ocean ridge from the behaviour of ridge-axis discontinuities, *Nature,* **335,** 217–225.

Macdonald, K.C., Scheirer, D.S. & Carbotte, S.M., 1991. Mid-ocean ridges: discontinuities, segments, and giant cracks, *Science,* **253,** 986–994.

Macdonald, K.C. *et al.*, 1992. The East Pacific Rise and its flanks 8–18°N: history of segmentation, propagation and spreading direction based on SeaMARC II and Sea Beam studies, *Mar. Geophys. Res.,* **14,** 299–344.
MacLeod, C.J. & Rothery, D.A., 1992. Ridge axial segmentation in the Oman ophiolite: evidence from along-strike variations in the sheeted dyke complex, in *Ophiolites and their Modern Analogues,* pp. 39–63, eds Parson, L.M., *et al.*, Geol. Soc. Spec. Publ. 60, London.
Madsen, J.A., Detrick, R.S., Mutter, J.C., Buhl, P. & Orcutt, J.A., 1990. A two- and three-dimensional analysis of gravity anomalies associated with the East Pacific Rise at 9°N and 13°N, *J. geophys. Res.,* **95,** 4967–4987.
Matsumoto, T., Hosford, A. & Dick, H.J.B., 2001. Gravity signal of the mantle exposure on the Atlantis Bank and the Atlantis-II fracture zone, Southwest Indian ridge (abstract), in *EGS XXVI General Assembly,* Nice, France.
Miller, D.J. & Christensen, N.I., 1997. Seismic velocities of lower crustal and upper mantle rocks from the slow spreading Mid-Atlantic Ridge, south of the Kane transform zone (MARK), *Proc. Ocean Drill. Program Sci. Results,* **153,** 437–454.
Moser, T.J., 1991. Shortest path calculation of seismic rays, *Geophysics,* **56,** 59–67.
Moser, T.J., Nolet, G. & Snieder, R., 1992. Ray bending revisited, *Bull. seism. Soc. Am.,* **82,** 259–288.
Nicolas, A., Boudier, F. & Ildefonse, B., 1996. Variable crustal thickness in the Oman ophiolite: implication for oceanic crust, *J. geophys. Res.,* **101,** 17 941–17 950.
Paige, C.C. & Saunders, M.A., 1982. LSQR: an algorithm for sparse linear equations and sparse least squares, *Trans. Math. Software,* **8,** 43–71.
Parmentier, E.M. & Phipps Morgan, J., 1990. Spreading-rate dependence of three-dimensional structure in oceanic spreading centers, *Nature,* **348,** 325–328.
Ross, W.S., 1994. The velocity–depth ambiguity in seismic traveltime data, *Geophysics,* **59,** 830–843.
Scheirer, D.S. & Macdonald, K.C., 1993. Variation in cross-sectional area of the axial ridge along the East Pacific Rise: evidence for the magmatic budget of a fast spreading center, *J. geophys. Res.,* **98,** 7871–7885.
Sempéré, J.-C. & Macdonald, K.C., 1986. Deep-tow studies of the overlapping spreading centers at 9°03′N on the East Pacific Rise, *Tectonics,* **5,** 881–900.
Sempéré, J.-C., Macdonald, K.C. & Miller, S.P., 1984. Overlapping spreading centers: 3-D inversion of the magnetic field at 9°03′N on the East Pacific Rise, *J. R. astr. Soc.,* **79,** 799–811.
Smith, W.H.F. & Wessel, P., 1990. Gridding with continuous curvature splines in tension, *Geophysics,* **55,** 293–305.
Tolstoy, M., Harding, A.J. & Orcutt, J.A., 1993. Crustal thickness on the Mid-Atlantic Ridge: bull's-eye gravity anomalies and focused accretion, *Science,* **262,** 726–729.
Toomey, D.R., Purdy, G.M., Solomon, S.C. & Wilcock, W.S.D., 1990. The three-dimensional seismic velocity structure of the East Pacific Rise near latitude 9°30′N, *Nature,* **347,** 639–645.
Toomey, D.R., Solomon, S.C. & Purdy, G.M., 1994. Tomographic imaging of the shallow crustal structure of the East Pacific Rise at 9°30′N, *J. geophys. Res.,* **99,** 24 135–24 157.
Toomey, D.R., Detrick, R.S. & Wilcock, W.S.D., 1997. Mapping melt and matrix flow in the uppermost mantle: undershooting the East Pacific Rise between the Siqueiros and Clipperton, *R/V Maurice Ewing Leg 97–08,* Cruise Rep., p. 163, Woods Hole Oceanogr. Inst., Woods Hole, MA.
Toomey, D.R., Wilcock, W.S.D., Detrick, R.S. & Dunn, R.A., 1998. Mapping melt and matrix flow in the uppermost mantle: preliminary results from undershooting the EPR, *EOS, Trans. Am. geophys.Un.,* **79**, Fall Meet. Suppl., F805.
van Avendok, H.J.A., Harding, A.J., Orcutt, J.A. & McClain, J.S., 1998. A two-dimensional tomography study of the Clipperton transform fault, *J. geophys. Res.,* **103,** 17 885–17 899.
van Avendok, H.J.A., Harding, A.J., Orcutt, J.A. & McClain, J.S., 2001. Contrast in crustal structure across the Clipperton transform fault from travel time tomography, *J. geophys. Res.,* **106,** 10 961–10 981.
Vera, E.E. & Diebold, J.B., 1994. Seismic imaging of oceanic layer 2A between 9°30′N and 10°N on the East Pacific Rise from two-ship wide-aperture profiles, *J. geophys. Res.,* **99,** 3031–3041.
Vera, E.E., Mutter, J.C., Buhl, P., Orcutt, J.A., Harding, A.J., Kappus, M.E., Detrick, R.S. & Brocher, T.M., 1990. The structure of 0- to 0.2-m.y.-old oceanic crust at 9°N on the East Pacific Rise from expanded spread profiles, *J. geophys. Res.,* **95,** 15 529–15 556.
Wang, X. & Cochran, J.R., 1993. Gravity anomalies, isostasy, and mantle flow at the East Pacific Rise crest, *J. geophys. Res.,* **98,** 19 505–19 351.
Wang, X., Cochran, J.R. & Barth, G.A., 1996. Gravity anomalies, crustal thickness, and the pattern of mantle flow at the fast spreading East Pacific Rise, 9°–10°N: evidence for three-dimensional upwelling, *J. geophys. Res.,* **101,** 17 927–17 940.
Wessel, P. & Smith, W.H.F., 1995. New version of the generic mapping tools released, *EOS, Trans. Am. geophys. Un.,* **76**, 329.
White, R.S., McKenzie, D. & O'Nions, R.K., 1992. Oceanic crustal thickness from seismic measurements and rare earth element inversions, *J. geophys. Res.,* **97,** 19 683–19 715.
Wilcock, W.S.D., Solomon, S.C., Purdy, G.M. & Toomey, D.R., 1992. The seismic attenuation structure of a fast-spreading mid-ocean ridge, *Science,* **258,** 1470–1474.
Wilcock, W.S.D., Solomon, S.C., Purdy, G.M. & Toomey, D.R., 1995. Seismic attenuation structure of the East Pacific Rise near 9°30′N, **100,** 24 147–24 165.
Zhang, J. & Toksöz, M.N., 1998. Nonlinear refraction traveltime tomography, *Geophysics,* **63,** 1726–1737.

APPENDIX A: RAY COVERAGE AND DATA FITTING

The crustal structure within the upper 3 km is constrained by the dense and well-distributed *Pg*-ray coverage, while the lower-crustal structure and the depth to the Moho are constrained by the *PmP* rays (Fig. A1). The fit between the observed and predicted traveltimes for each instrument in the outer profiles is shown in Figs A2 and A3, and the reduction in rms and χ^2 is listed in Table A1.

Figs A4–A7 show the *PmP* rays and their associated traveltime curves predicted by the preferred models for some selected instruments that sample the main features of the Moho. We compare these predicted traveltimes with the observed record sections and interpreted picks, and with the predicted *PmP* traveltime curves obtained from forward modelling two hypothetical models consisting of our preferred velocity structures and constant crustal thickness of 6 and 7 km. The examples that we discuss in the following paragraphs show that if our preferred crustal velocity structures are well constrained, a model with constant crustal thickness (either 6 or 7 km) cannot explain successfully all the data, demonstrating that crustal thickness variations are required by the data. The trade-off between crustal velocity anomalies and crustal thickness variations is further discussed in Appendix B.

Along the southernmost section of the outer western line (Fig. A4a), crustal thinning towards the north between –80 and –50 km model distance is required, for example, by OBS 58 and OBH 16. A model with a crustal thickness of 7 km is consistent with the observed *PmP* traveltimes in OBS 58 (Fig. A4b), but it overestimates the *PmP* traveltimes for OBH 16 (Fig. A4c). In comparison, a model with 6 km crustal thickness fits the data from OBH 16, but underestimates the traveltimes for OBS 58. The thick crust found in the middle section of this profile (near 0 km model distance, Fig. A4a) is required by instruments such as OBS 55. Neither the 6 km or the 7 km crustal thickness models can explain the *PmP* traveltimes observed at this instrument (Fig. A4d), confirming the >7 km thick crust obtained from the inversion in this section of the profile. The crustal thickness along the northern segment (20–30 km model distance) is close to 7 km, as shown in Fig. A4(e) where data from instrument OBH 27 are consistent with the 7 km crustal thickness

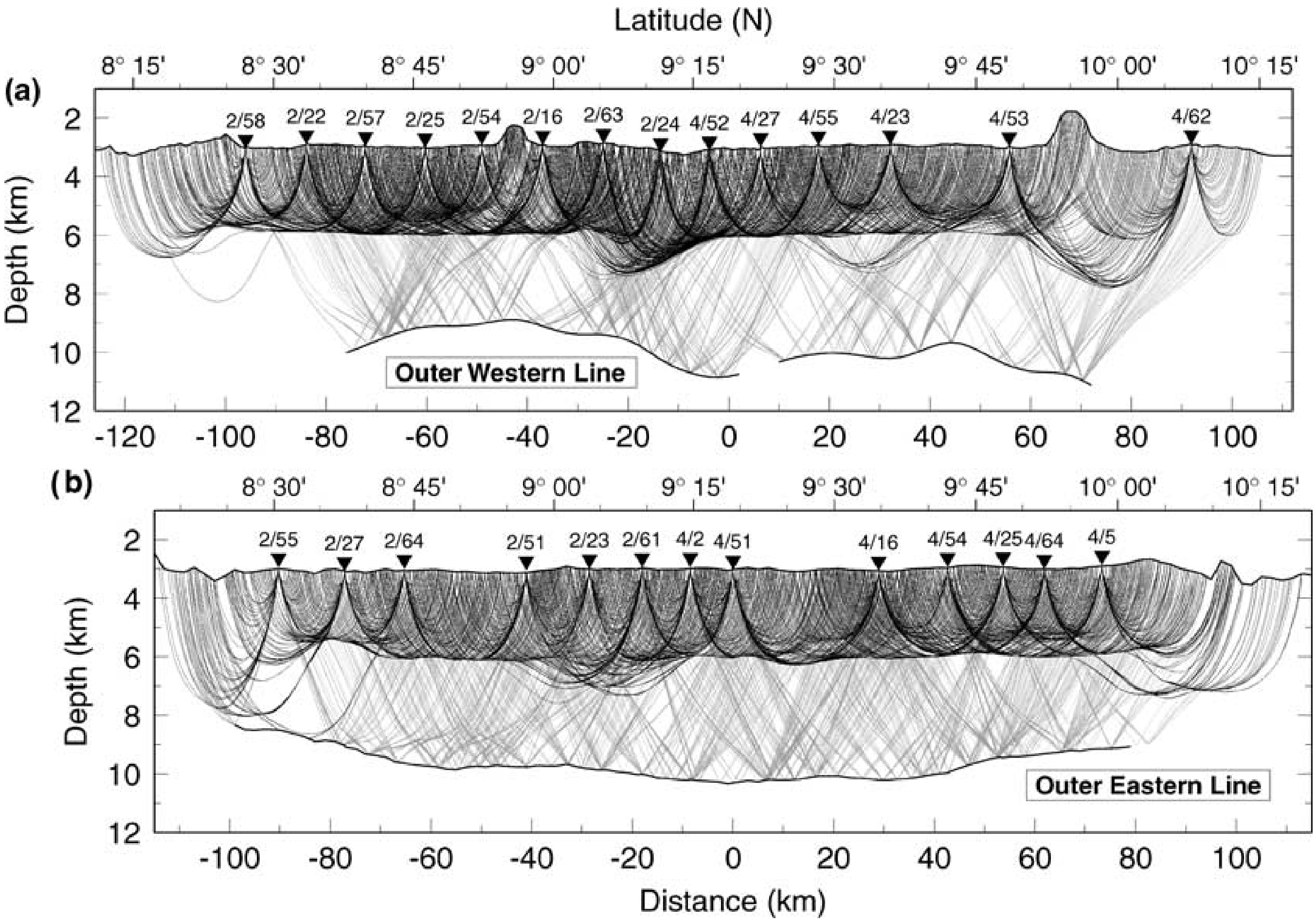

Figure A1. *Pg* ray (dark) and *PmP* ray (light grey) density for: (a) outer western line and (b) outer eastern line. The scales, labelling and solid line are as in Fig. 5.

model while the 6 km crustal thickness model underestimates the *PmP* traveltimes.

Along the outer eastern line, the crustal thickness variation at the southern segment (Fig. A5a) is illustrated by OBS 55, where the observed *PmP* traveltimes are consistent with the 6 km crustal thickness model but not with the 7 km model (Fig. A5b), and by OBH 23 where the observed *PmP* traveltimes are in between those predicted by the constant crustal thickness models (Fig. A5c). *PmP* arrivals from ORB 2, located near the centre of the profile, are better explained by the 7 km crustal thickness model rather than the 6 km model (Fig. A5d), while data from OBS 54 requires thinner crust at the northern end of the profile (Fig. A5e).

The progressive thickening of the crust towards the south along the inner eastern line is shown in data from instruments OBS 60 and OBH 24 (Fig. A6). *PmP* arrivals from OBS 60 (Figs A6b and c) and the southern side of OBH 24 (Fig. A6d) are consistent with a 7 km thick crust, while *PmP* arrivals from the northern side of OBH 24 (Fig. A6e) are consistent with a 6 km thick crust. Also, the crustal thickening towards the rise axis along the EPR-5 line (Fig. A7a) is apparent in *PmP* arrivals from instruments located near the rise axis (OBH 26 and OBS 61, Figs A7(c) and (d), respectively) which require $\geq$7 km thick crust, while data from instruments located in older crust (OBS 56 and ORB 3, Figs A7b and e, respectively) indicate thinner crust.

Table A1. Root-mean-square (rms) and χ^2 misfit parameter between the observed and predicted traveltimes for the initial and best-fitting models.

Line	Initial rms			Best-fit rms			Initial χ^2			Best-fit χ^2		
	Pg	*PmP*	*Both*	*Pg*	*PmP*	*Both*	*Pg*	*PmP*	*Both*	*Pg*	*PmP*	*Both*
Outer western	122	197	144	25	28	26	23.8	62.3	33.2	1.0	1.2	1.0
Inner western	84	103	89	29	24	28	11.3	17.1	12.7	1.3	0.9	1.2
Inner eastern	112	85	104	27	22	26	20.1	11.5	17.5	1.2	0.8	1.1
Outer eastern	86	60	82	23	25	24	11.9	5.7	10.7	0.9	1.0	0.9
West EPR-5	81	131	104	30	24	28	10.5	27.4	17.2	1.5	0.9	1.2
East EPR-5	76	86	80	28	24	27	9.3	12.1	10.2	1.3	0.9	1.2
West EPR-1	82	91	85	27	27	27	10.7	13.3	11.7	1.1	1.2	1.1
East EPR-1	87	84	86	37	22	32	12.3	11.4	11.9	2.3	0.8	1.7

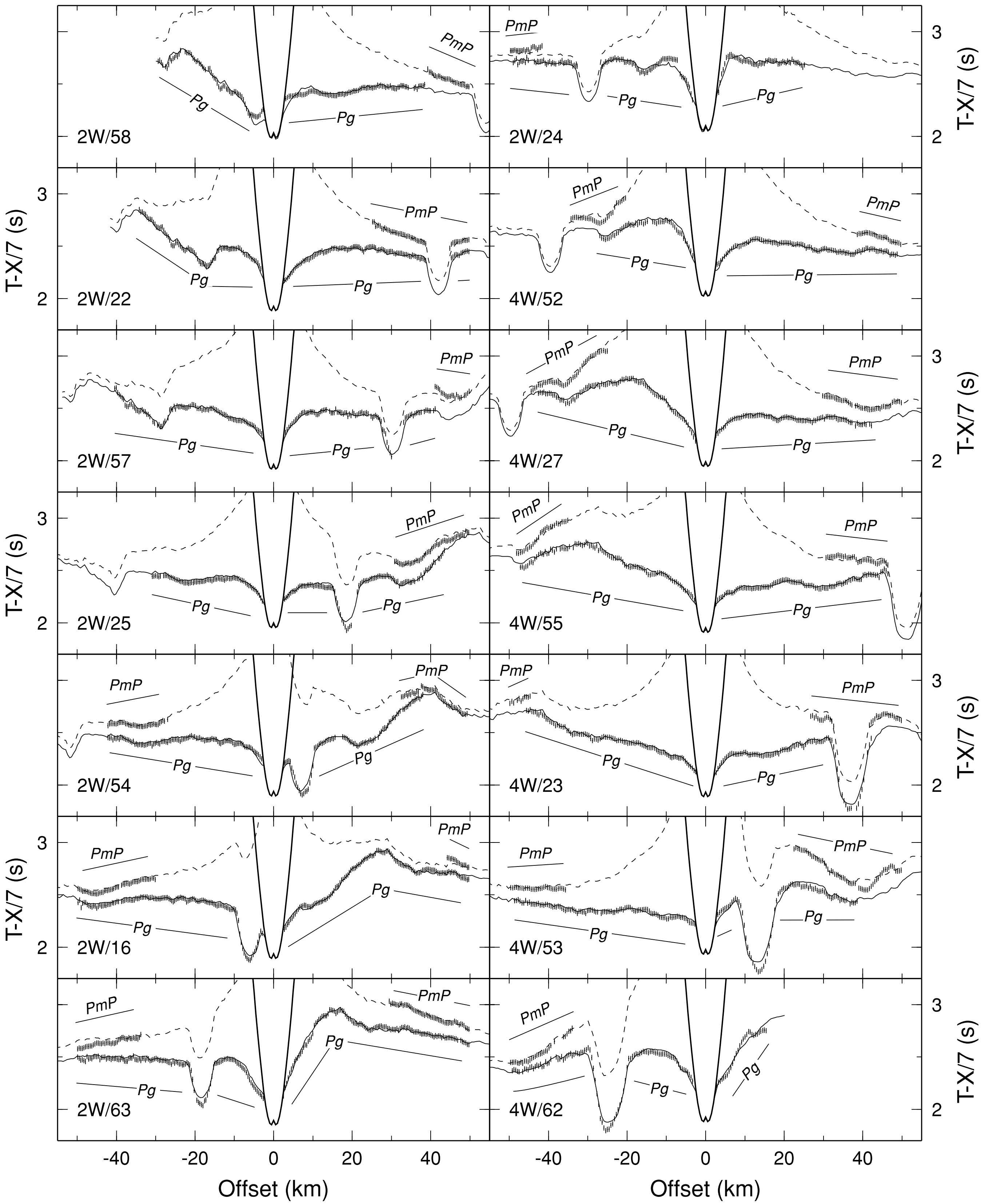

Figure A2. Observed (vertical bars) and predicted (solid line for *Pg,* dashed line for *PmP*) traveltimes for each of the instruments along the outer western profile. The thick solid line is the traveltime curve of the direct wave.

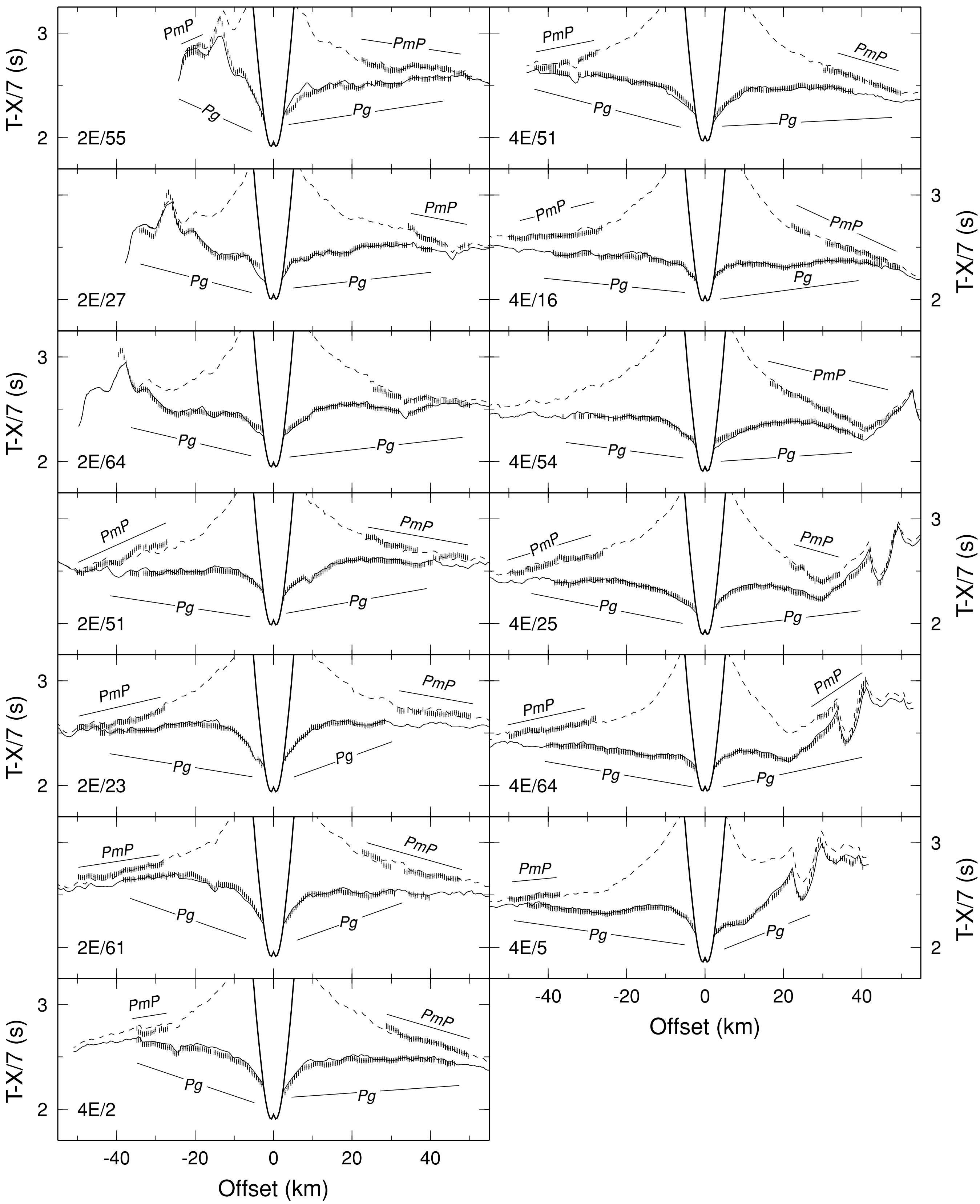

Figure A3. Same as in Fig. A2 but for the instruments along the outer eastern profile.

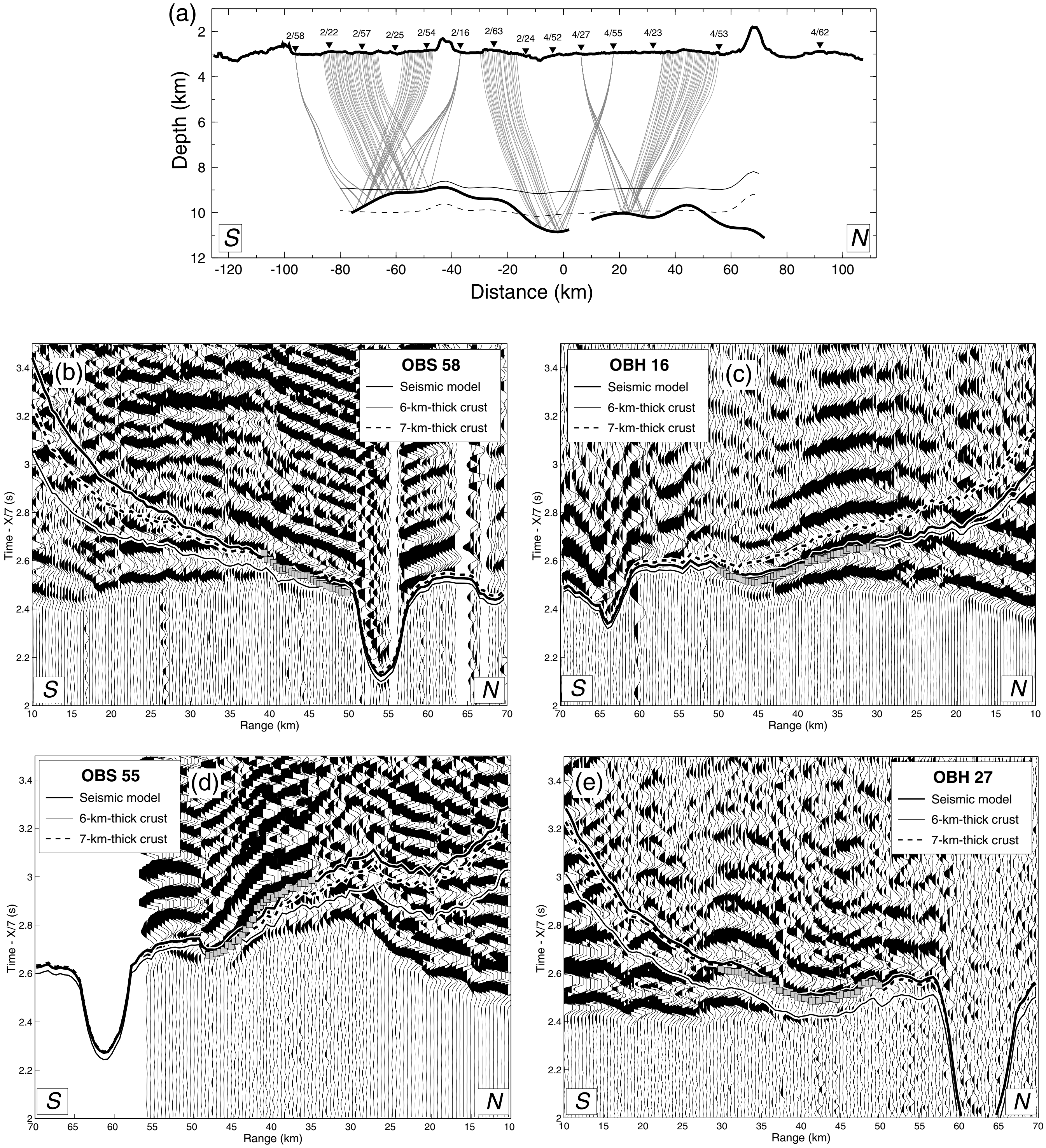

Figure A4. (a) Selected *PmP* rays sampling the best-fitting Moho (thick solid line) along the outer western line for four selected instruments. Thin solid and dashed lines show the Moho for the hypothetical cases of constant crustal thickness of 6 and 7 km, respectively. (b) Seismograms from the southern instrument OBS 58 of the outer western line showing the traveltime picks for the *PmP* phase (grey squares) and the *PmP* traveltime curve predicted by the best-fitting seismic model (thick solid line). Thin solid and thick dashed lines are the *PmP* traveltime curves predicted by models with constant crustal thickness of 6 and 7 km, respectively. (c), (d) and (e) as in (b) for OBH 16, OBS 55 and OBH 27, respectively.

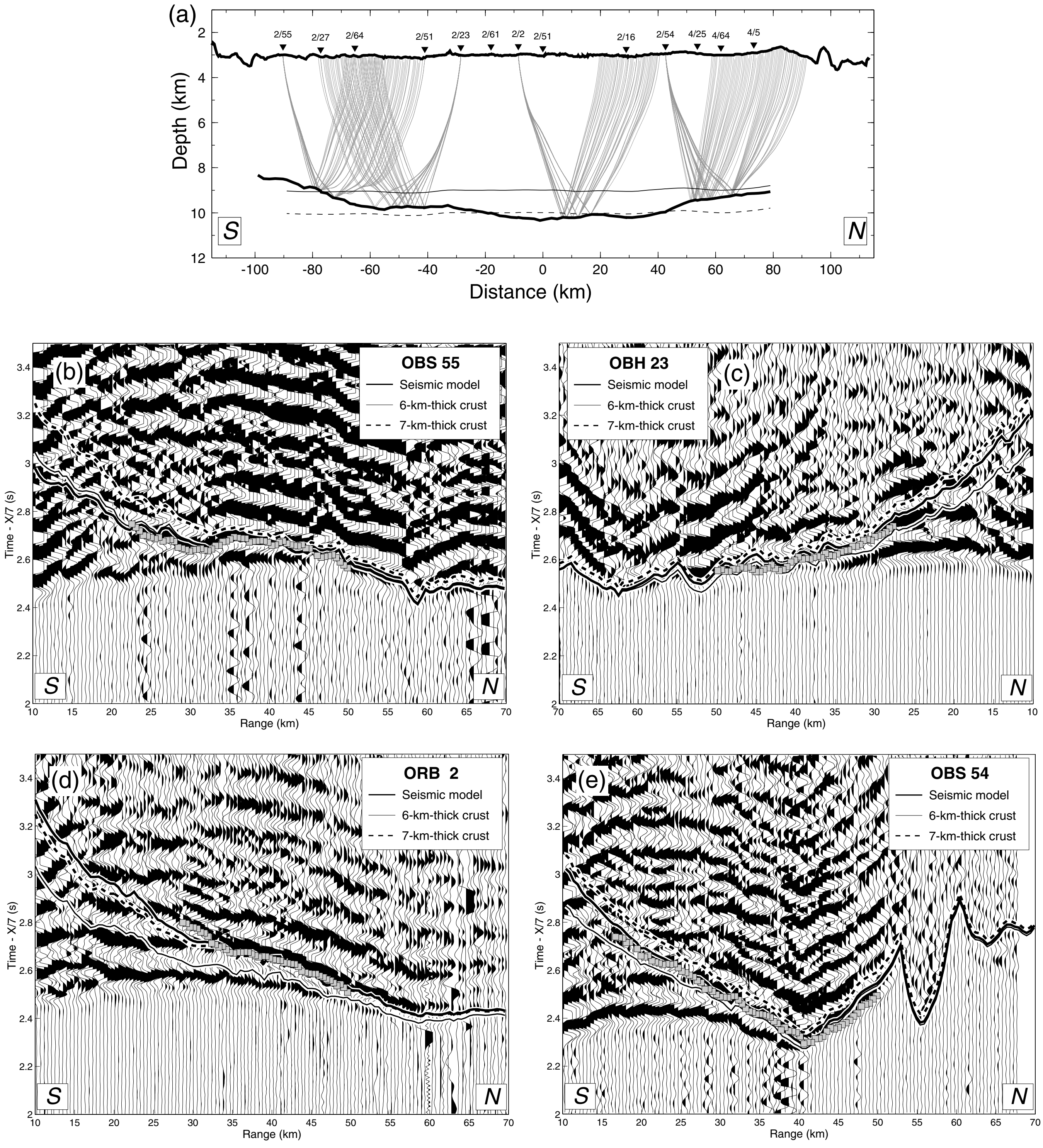

Figure A5. Same as in Fig. A4 showing (a) selected *PmP* rays along the outer eastern line for instruments (b) OBS 55, (c) OBH 23, (d) ORB 2 and (e) OBS 54.

APPENDIX B: RESOLUTION TESTS AND THE DEPTH–VELOCITY AMBIGUITY

To assess the resolution of our results we performed several tests. First, we reconstructed synthetic models along the outer lines and EPR-5 using a chequerboard pattern of velocity anomalies and a sinusoidal perturbation in the Moho. We also tested synthetic models of layer 2A thickening as a plausible source contributing to the low-velocity anomaly at ~9°10′N in the outer western line. Finally, we explored the ambiguity between lower-crustal velocity anomalies and crustal thickness variations using isolated synthetic anomalies within the lower crust and perturbations in the Moho depth.

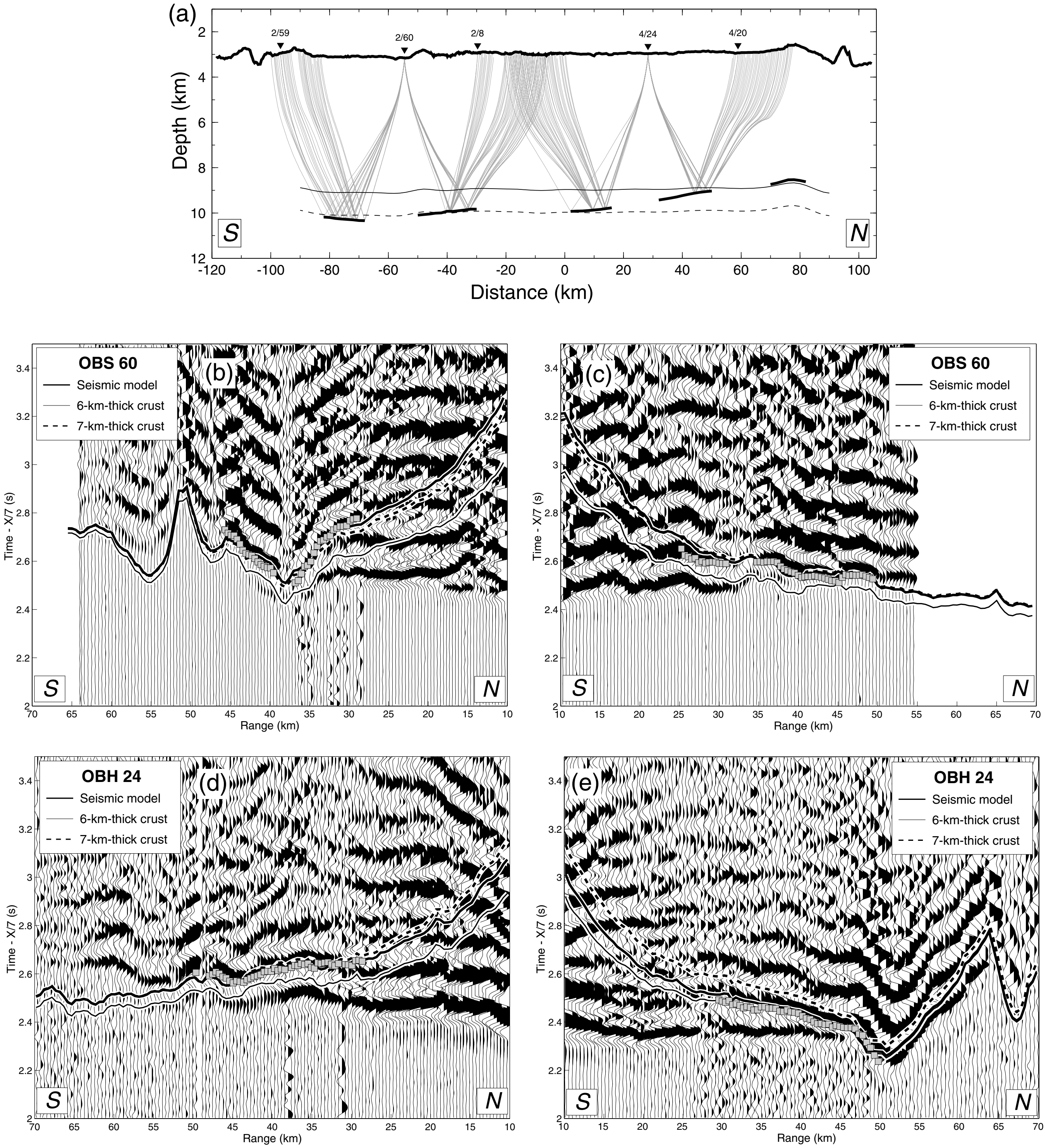

Figure A6. Same as in Fig. A4 showing (a) selected *PmP* rays along the inner eastern line for instruments (b) south-looking OBS 60, (c) north-looking OBS 60, (d) south-looking OBH 24 and (e) north-looking OBH 24.

For the chequerboard tests we added velocity perturbations of ± 5 per cent with respect to a 1-D velocity structure (Fig. 4) in 20×2 km^2 cells, alternating positive and negative anomalies. The synthetic Moho was constructed by imposing a sinusoidal variation of 1 km in amplitude upon a 6 km crustal-thickness Moho, with a half-wavelength of $\sim$60 and $\sim$33 km along the outer lines and EPR-5, respectively. The *Pg* and *PmP* traveltimes predicted by the synthetic models (for the same shot–receiver configuration as in our experiment) were perturbed with a common-receiver random Gaussian noise distribution $N(0, \sigma = 10$ ms) and a random Gaussian perturbation $N(0, \sigma = 15$ ms km^{-1}) to the traveltime gradients, following the method of Zhang & Toksöz (1998). We then inverted the synthetic data using the same model parametrization, initial velocity model, and initial Moho depth as in our preferred solutions.

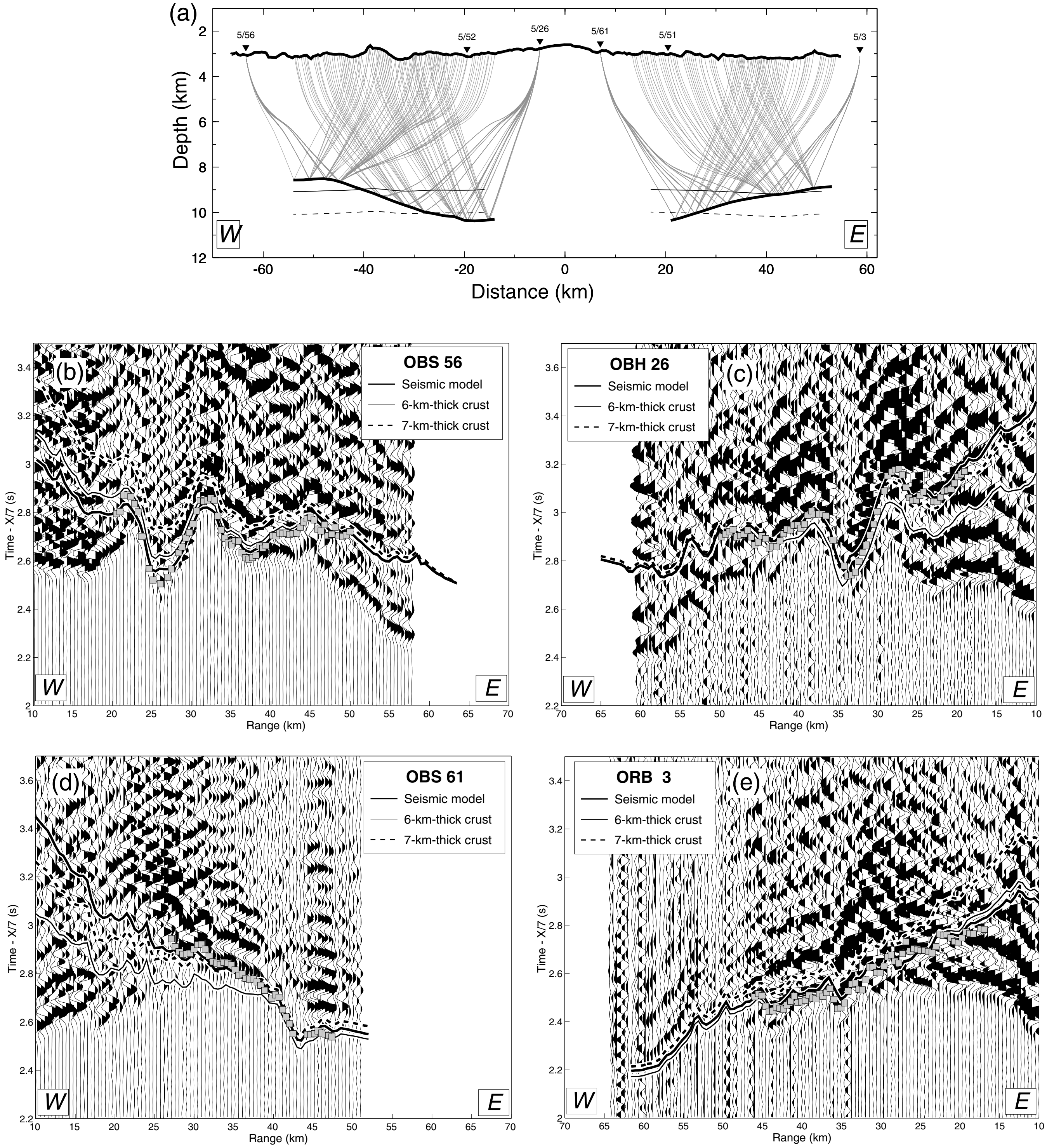

Figure A7. Same as in Fig. A4 showing (a) selected *PmP* rays along the line EPR-5 for instruments (b) OBS 56, (c) north-looking OBH 26, (d) OBS 61 and (e) north-looking ORB 3.

The reconstructed anomalies (Fig. B1) are remarkably good within the upper 4 km of the crust owing to the high density of *Pg* rays (Fig. A1). The tests show that the vertical resolution of our preferred solutions (Figs 5 and 6) is 2 km, and that the tomographic inversion underestimates the amplitude of the anomalies, especially within the upper 2 km. Although tests with thinner velocity anomalies provided acceptable results in some parts of the profiles, we adopted a conservative estimate of 2 km as the average vertical resolution for all the profiles. The chequerboard test cannot resolve anomalies within the lower crust. This reflects the inherent limitation of chequerboard tests, which do not simulate realistic patterns of velocity anomalies in the Earth, and provide an estimate of the average coarsest resolution of the model. The tests also show that the data can effectively detect variations in Moho depth $\geq$1 km along

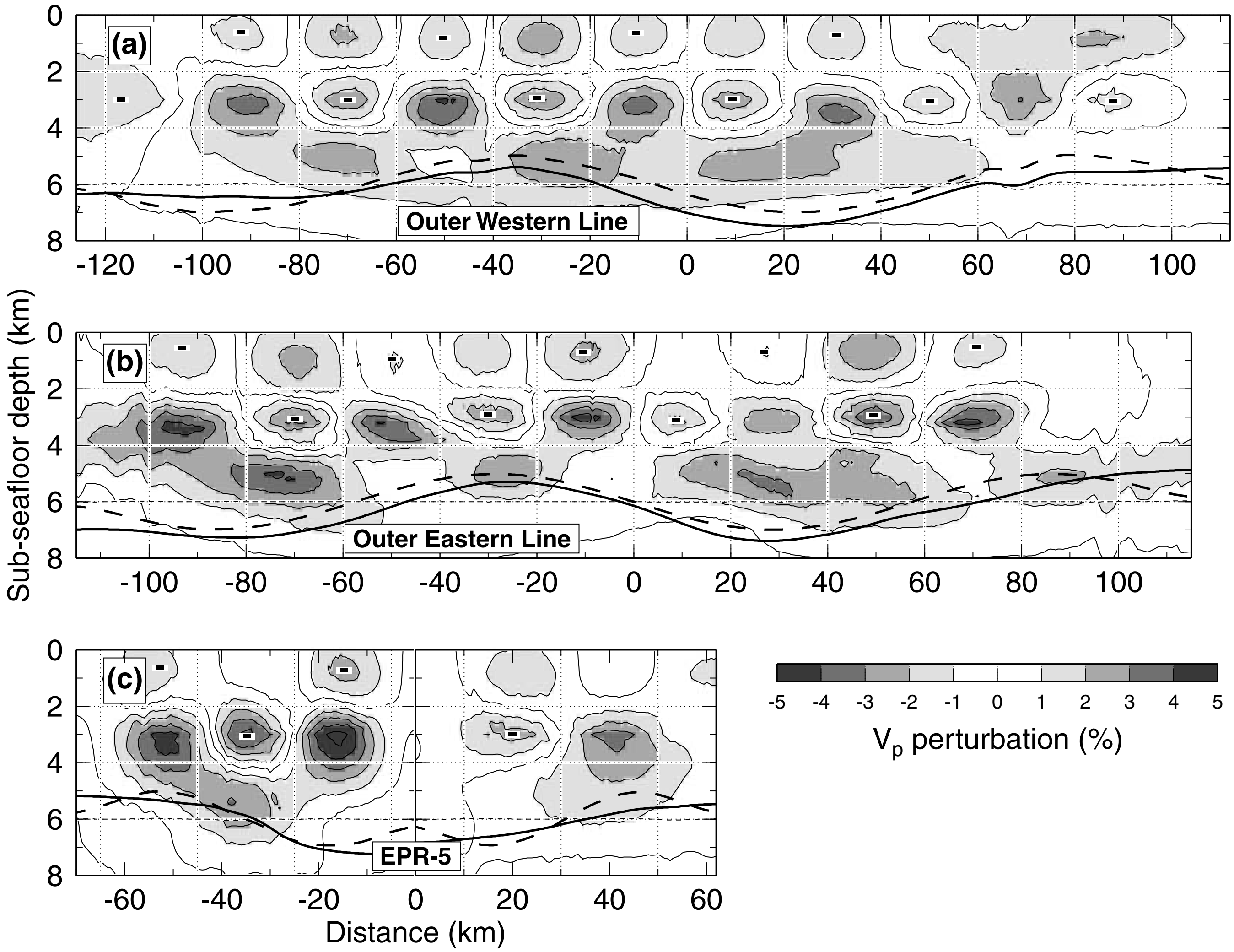

Figure B1. Chequerboard resolution test for: (a) outer western line, (b) outer eastern line and (c) EPR-5. Shaded anomalies are the recovered velocity perturbations (in per cent), contoured every 1 per cent (negative anomalies are marked with the symbol '-'). The dotted grid bounds the position of the original anomalies, which were given maximum amplitudes of ±5 per cent with respect to a 1-D velocity model (Fig. 4). Also shown is a resolution test for a sinusoidal perturbation in the Moho (thick dashed line). The solid line is the recovered Moho, and the thin dashed line is the initial Moho (6 km constant crustal thickness). Both the chequerboard anomalies and the perturbed Moho were inverted simultaneously.

the profiles at wavelengths similar to that of the observed crustal thickness variations (Figs 5 and 6), although the absolute crustal thickness is generally overestimated. This is probably related to the limitation of the test to detect lower-crustal velocity anomalies, and to the velocity–depth trade off. Resolution within the lower crust and the depth–velocity ambiguity are discussed later in the text.

Although our most conservative estimate of the vertical resolution is 2 km, we tested whether an increase in layer 2A thickness from 0.4 km (Christeson *et al.* 1994) to 1 km (Bazin *et al.* 2001) within overlap basin 3 could contribute to the low-velocity anomaly observed beneath the basin (Fig. 5e). We tested two different synthetic models. In one case (model 1), velocities typical of layer 2A were extended down to 1 km below the seafloor, and the deeper structure remained unperturbed (Figs B2a and e). In the second case (model 2) we added 0.6 km of low-velocity material (2.6 km s^{-1}) to the top of the reference model, therefore depressing the velocities from the seafloor down to the Moho (Figs B2c and e). As in the chequerboard tests, we added noise to the traveltimes predicted by the synthetic models, and inverted them using the same model parametrization as in our preferred solution. We found that the reconstructed anomalies (Figs B2b and d) have the same lateral extent as the original ones, although with lower amplitudes. Some smearing occurs down to 2 km below the seafloor in the first case (Fig. B2b) and to 3 km in the second model (Fig. B2d). Fig. B2(e) shows the recovered velocity structures for both cases, compared with the velocity structure found beneath overlap basin 3 (Fig. 4). The close similarity between the results of synthetic model 2 with those obtained along the outer western profile near 9°10′W suggests that the emplacement of ~600 m of extrusive lavas on top of the crust in the overlap basin is sufficient to explain the negative velocity anomaly found beneath overlap basin 3.

Since the velocity structure of the lower crust and the depth to the Moho are both determined from the *PmP* traveltimes, some ambiguity between velocity and depth may exist (e.g. Ross 1994). We explored this trade off in our solutions and the resolution of the velocity models within the lower crust using isolated, synthetic velocity anomalies located above sections of thicker and thinner crust. We tested 20 × 2 km^2 blocks with ±5 per cent of velocity

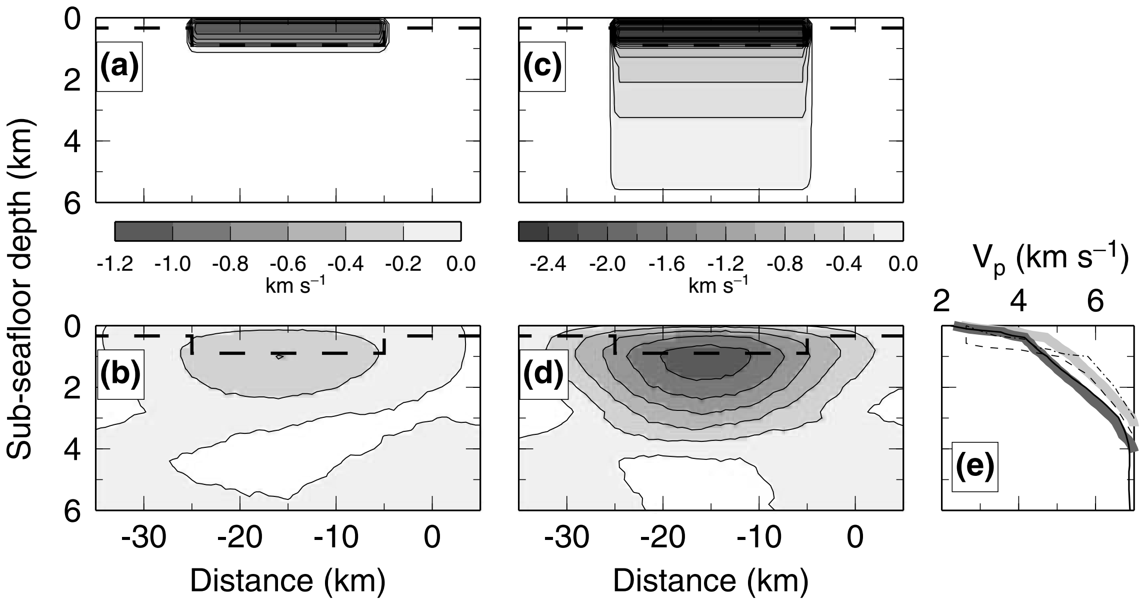

Figure B2. Synthetic velocity anomalies for tests of layer 2A thickening from 0.4 to 1 km between −25 and −5 km model distance along the outer western line. The dashed line indicates the base of layer 2A. Contours are every 0.2 km s^{-1}. (a) Model 1: velocities typical of layer 2A extend down to 1 km below the seafloor. (b) Recovered anomaly after inverting the traveltimes predicted by the model in (a) using the shot–receiver configuration of the outer western line. (c) Model 2: a 0.6 km thick low-velocity layer is added to the top of the reference model, depressing the seismic velocities down to the base of the crust. (d) Recovered anomaly for model in (c). (e) True (dot-dashed) and recovered (light grey) velocity structures for model 1; and true (dashed) and recovered (dark grey) velocity structures for model 2. Solid line is the velocity structure obtained along the outer western profile at 9°10′N beneath the relict overlap basin 3 as in Fig. 4. Note how the solution of synthetic model 2 resembles the structure beneath the overlap basin.

perturbation with respect to a 1-D velocity structure. We considered all possible combinations of positive and negative velocity anomalies located above thick and thin crust (Fig. B3). Before the inversion, the traveltimes predicted by the synthetic models were perturbed with random noise as in the chequerboard tests. The results show that the data can detect positive anomalies in the lower crust along the three profiles, and that the depth to the Moho beneath the positive anomalies is always well recovered (Fig. B3). The test resolves the size of lower-crustal negative anomalies along the outer lines (Figs B3a–d) and underestimates their amplitude, but it fails to detect such anomalies along EPR-5 (Fig. B3e). The depth to the Moho beneath negative anomalies is well resolved if the anomalies overlay sections of thick crust (Figs B3b and d), but it is overestimated by ∼1 km if the negative anomalies are above sections of thin crust (Figs B3a, d and e).

This test shows that it is possible that the crustal thickness in our preferred solutions is overestimated if there are low-velocity anomalies within the lower crust. This case would apply to the thick crust found along the outer western line between 9°10′N and 9°20′N, where a 0.2–0.4 km s^{-1} negative anomaly is present in the lower crust (Fig. 5e), or to the thick crust along EPR-5 between 104°30′W and 104°20′W, which is overlain by a −0.2 km s^{-1} lower-crustal velocity anomaly. We explored the magnitude of the lower-crustal velocity anomalies that would be required to fit the observed traveltimes if there were not significant changes in crustal thickness along the profiles. The weighting of the depth kernel (w) controls the degree of perturbation of the floating-reflector depth nodes with respect to the velocity nodes (Korenaga *et al.* 2000). We found that our results are not significantly sensitive to the value of w, except for very low values of w. In such a case, we found that inverting the data with $w = 0.01$ results in an acceptable solution that fits the data with the same degree of accuracy as our preferred models. The solution for $w = 0.01$ has large lateral velocity variations (>1.2 km s^{-1}) within the lowermost 2 km of the crust, and a constant crustal thickness of 6 km. Such velocity variations are much larger than the range of V_p variability measured in oceanic gabbros (0.6 km s^{-1}) (Iturrino *et al.* 1991; Miller & Christensen 1997), and if real, they would require the presence of fluids in the lowermost crust. An independent study of the crustal shear velocity structure (which is most sensitive to the presence of fluids) in this same area using seafloor compliance methods suggests that the lower crust has a normal shear structure (free of fluids) at distances >7 km from the rise axis (Crawford & Webb 2002). Thus we conclude that the crustal thickness variations shown in Figs 5 and 6 are real and not an artefact of the method owing to the hypothetical presence of abnormally low velocities within the lower crust.

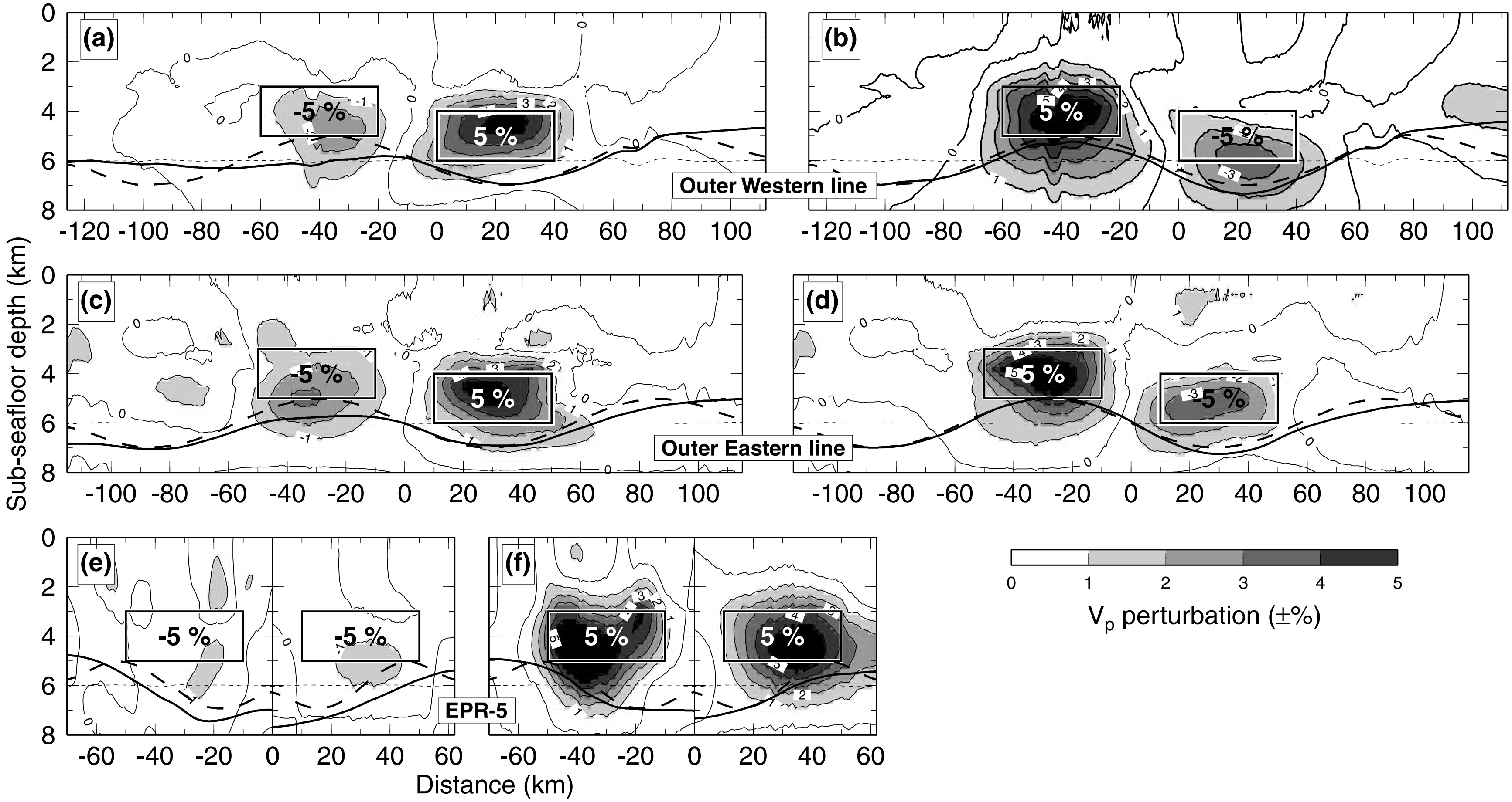

Figure B3. Resolution tests for the lower crust and the trade-off between lower-crustal velocities and crustal thickness. Rectangles show the location of the synthetic velocity anomalies. Recovered velocity anomalies (shaded) are contoured every 1 per cent. A sinusoidal perturbation was added to the Moho depth (thick dashed line). The solid line is the recovered Moho, and the thin dashed line is the initial Moho (6 km constant crustal thickness). (a) Case where a positive lower-crustal velocity anomaly sits above a section of thick crust, and a negative lower-crustal velocity anomaly sits above a section of thin crust for the outer western line. (b) Same as (a) but with the opposite relation between velocity anomalies and crustal thickness. (c) and (d), same as (a) and (b), respectively, for the outer the eastern line. (e) Case where negative lower-crustal velocity anomalies sit above thick crust for profile EPR-5. Note that the synthetic tests east and west of the rise axis (0 km model distance) were done independently from each other (therefore the discontinuity in contouring and Moho depth at $X = 0$ km). (f) Same as (e) for positive velocity anomalies.